Quaternary Science Reviews 357 (2025) 109310

Contents lists available at ScienceDirect

Quaternary Science Reviews

journal homepage: www.elsevier.com/locate/quascirev

Coupled sea-level and hydroclimatic controls on the southern Red Sea sedimentation during the past 30 ka

Francesca Paraschos [a,b,*], Andreas Koutsodendris [c], Spyros Sergiou [b], Maria Geraga [b], Helen Kaberi [a], Melissa Berke [d], Oliver Friedrich [c], Stylianos Iliakis [a], Mirko Alessandro Uy [d], Ross Williams [d], Geoffrey Bailey [e,f], Dimitris Sakellariou [a]

[a] Institute of Oceanography, Hellenic Centre for Marine Research, Athens-Sounio Ave 46.7km, 19013, Athens, Greece
[b] Laboratory of Marine Geology and Physical Oceanography (Oceanus-Lab), Department of Geology, University of Patras, 26504, Patras, Greece
[c] Institute of Earth Sciences, Heidelberg University, Im Neuenheimer Feld 234-236, 69120, Heidelberg, Germany
[d] Department of Civil and Environmental Engineering and Earth Sciences, University of Notre Dame, 156 Fitzpatrick Hall, Notre Dame, IN, 46556, USA
[e] Department of Archaeology, King's Manor, University of York, York, YO1 7EP, United Kingdom
[f] College of Humanities, Arts and Social Sciences, Flinders University, Adelaide, Australia

A R T I C L E I N F O

Handling editor:Dominik Fleitmann

Keywords:
Southern Red Sea
Sea-level changes
Glacial period
African Humid Period
Detrital grain size distribution
Sediment geochemistry
Plant wax biomarkers

A B S T R A C T

Sedimentation in the Red Sea basin is governed by the complex interplay between regional atmospheric circulation, precipitation patterns, and sea level fluctuations, which altogether exert a profound control on the detrital and biogenic components of the sedimentary record. To gain a comprehensive understanding of these controls on the southern Red Sea sedimentation over the past 30 ka, we here combine high-resolution bulk geochemical and mineralogical data with detrital grain-size distributions and plant-wax biomarkers at a sub-centennial average temporal resolution. Our proxies reveal that the sedimentary record is characterised by two distinct depositional regimes of detrital and marine origin. The pronounced shift from the detrital-dominated (ca. 30–14.6 kyr) to the marine-dominated phase (ca. 14.6–0.8 kyr) coincides with the end of Heinrich Event 1 and the rapid sea-level rise associated with Meltwater Pulse 1a. Flooding of the shelf during deglacial sea-level rise increased the distance between the core site and the respective shoreline, and partially controlled the delivery of detrital material to the site. Shifts in detrital grain-size distribution and mineralogical composition indicate a reduction in regional continental aridity and potentially weaker wind circulation with the onset of Greenland Interstadial-1, while the reestablishment of water-mass exchange with the Gulf of Aden from ca. 15 ka onwards led to a marine productivity surge at our study area. An increase of fine-grained fluvial material and terrestrial *n*-alkanes between ca. 16 and 8 ka points to the establishment of more pluvial conditions and the activation of local wadi runoff during the African Humid Period. Finally, the subtle but steady increase of detrital input from ca. 5 ka onwards suggests the re-establishment of continental aridity during the late Holocene.

1. Introduction

Anthropogenically induced climate change has already had a profound impact on the world's oceans (Belkin, 2009; Doney et al., 2012), while the predicted temperature increases over the coming decades are expected to rapidly modify sea level and ocean biogeochemistry (Bindoff et al., 2007; Doney et al., 2009). The impact of this warming trend on the global hydrological cycle is also expected to be severe (Douville et al., 2022), with studies suggesting that dry desert-like regions will become dryer, while wet tropical regions will get wetter (Held and Soden, 2006). Effects like these can be especially pronounced in semi-enclosed basins and coastal regions such as the Red Sea basin, where climate-change related phenomena tend to occur at a faster rate than average (e.g., Raitsos et al., 2011; Williams, 2013).

The Red Sea basin (Fig. 1) has long been established as a sensitive recorder of past oceanographic and hydroclimatic fluctuations. Its semi-enclosed nature has been exploited to refine models of sea-level change and shoreline migration over the past half million years (Arz et al., 2007; Grant et al., 2012; Grant et al., 2014; Lambeck et al., 2011; Rohling et al., 1998, 2013; Siddall et al., 2003, 2004). Across glacial-interglacial

* Corresponding author. Institute of Oceanography, Hellenic Centre for Marine Research, Athens-Sounio Ave 46.7km, 19013, Athens, Greece.
E-mail address: fparaskos@hcmr.gr (F. Paraschos).

https://doi.org/10.1016/j.quascirev.2025.109310
Received 19 September 2024; Received in revised form 1 March 2025; Accepted 9 March 2025
Available online 8 April 2025

transitions, pronounced shifts in regional atmospheric circulation and hydrological regimes have significantly influenced the source and transport mechanisms of detrital material (e.g., Stein et al., 2007). More specifically, Red Sea detrital input is primarily controlled by the complex interplay between the low-altitude wind and precipitation of the seasonally-reversed African (ASM) and Indian (ISM) summer monsoon systems (Nicholson, 2018; Rohling et al., 1998; Sirocko et al., 1993), and the mid-tropospheric mid-latitude westerlies (MLW; Develle et al., 2011; Ehrmann et al., 2024; Rojas et al., 2019) (Fig. 2). Over orbital timescales, insolation driven displacements of the Intertropical Convergence Zone (ITCZ) influence the spatial extent and intensity of the African and Indian monsoon systems, leading to periods of increased precipitation and savanna expansion across the North African and Arabian Deserts with implications for human settlement and dispersal (Crocker et al., 2022; Enzel et al., 2015; Fleitmann et al., 2011; Larrasoaña et al., 2003, 2013; Nicholson, 2018; Nicholson et al., 2020). The most recent of these wet periods, i.e., the last African Humid Period (AHP), occurred between ca. 15 and 5 ka, leading to an expansion of vegetation across the Saharan-Arabian Desert belt and a reduction in aeolian dust input into adjacent marine environments (Berke et al., 2012; Blanchet et al., 2024; Gasse, 2000; Lézine et al., 2014; Shanahan et al., 2015; Tierney and DeMenocal, 2013).

The Red Sea basin and the adjacent Arabian Peninsula have also emerged as key areas for the investigation of early human dispersals out of Africa and the influence of climate change on patterns of dispersal and demographic change. These studies have focussed on two primary climatic processes: (i) the periodic greening of the Sahara and Arabian Deserts which would have opened up the interior to human settlement and dispersal (Groucutt et al., 2015; Jennings et al., 2015; Parton et al., 2018; Petraglia et al., 2019), and; (ii) the lowering of sea level which would have facilitated sea crossings at the southern Red Sea during maximum regression, and exposed an extensive lowland territory as a potential refugium for human settlement and coast-wise dispersal during periods of maximum climatic aridity (Bailey et al., 2015, 2019; Faure et al., 2002; Sakellariou et al., 2019). The geoarchaeological significance of these areas further emphasises the need for improvements in the temporal and spatial resolution of regional palaeoclimatic records.

A considerable number of studies have focused on reconstructing the late Quaternary continental hydroclimate controls on the northern and central Red Sea sedimentation. These studies have relied on radiogenic isotope compositions and mineralogy (Hartman et al., 2020; Palchan et al., 2013; Stein et al., 2007), ^{230}Th-normalized mass accumulation rates (Palchan and Torfstein, 2019), sedimentary Ti/Ca ratios (Roberts et al., 2011), foraminiferal Mg/Ca compositions (Hartman et al., 2020) and grain-size distributions (Ehrmann et al., 2024; Palchan et al., 2013) in order to explore the provenance and weathering of detrital input and thereby decipher regional atmospheric circulation patterns. The regional hydroclimatic imprint on the southern Red Sea sedimentation, however, remains largely unexplored. To the best of our knowledge only a couple of studies have explored these controls through the use of Sr and Nd isotopic compositions, mineralogy, grain-size distributions and magnetic concentrations (Bouilloux et al., 2013a, 2013b; Rojas et al., 2019). Disentangling hydroclimatic imprints on sedimentation in the southern Red Sea can pose challenges due to the extensive, shallow continental shelf and its proximity to the Gulf of Aden, both of which amplify the effects of sea-level fluctuations and influence the detrital signal.

In light of the above, we here present a high-resolution multiproxy record of the marine sediment Core FA09 that was recovered at a 302 m water depth near the Farasan Islands, in the southern Red Sea (Fig. 1). Core FA09 is optimally situated at the edge of the southeastern continental shelf (Sakellariou et al., 2019) and is therefore a highly sensitive recorder of sea-level fluctuations and variations in the extent of the exposed continental shelf. It lies within the coastal region of SW Saudi Arabia; an ecologically diverse area of the Arabian Peninsula which receives relatively high rainfall, and is placed near the current northernmost position of the ISM (Clemens and Prell, 1990; Enzel et al., 2015; Fleitmann et al., 2003, 2007; Gasse, 2000). Furthermore, the region has

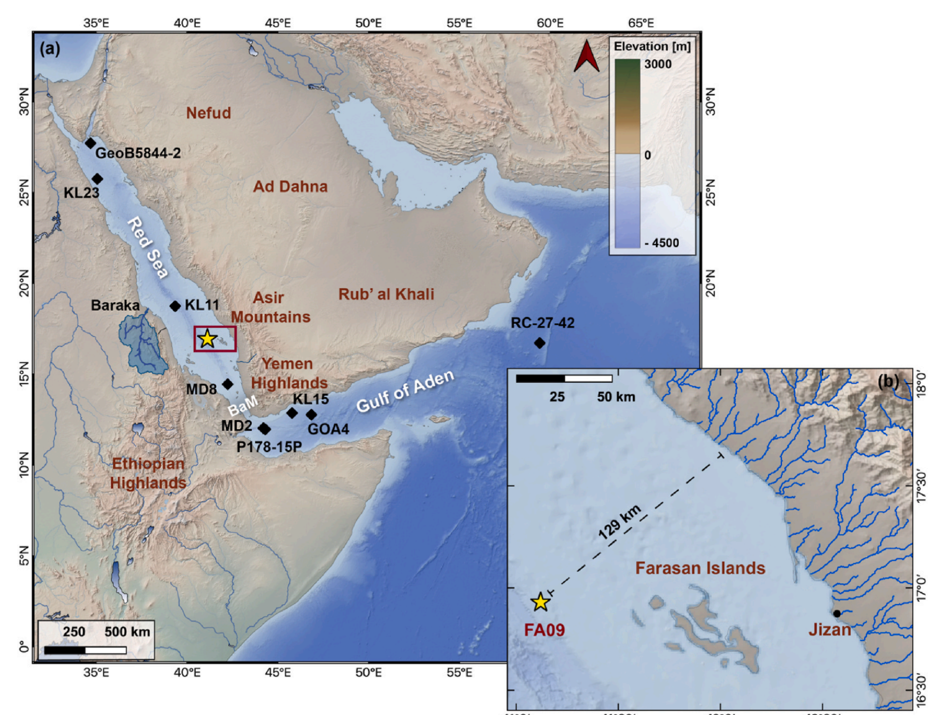

Fig. 1. (a) Map of the Red Sea and the surrounding regions including distinct features mentioned in the text. The locations of all discussed reference cores are marked with black diamonds while the yellow star marks the location of Core FA09. The dark red rectangle denotes the area shown in the close-up. (b) Close-up of our study area, including Core FA09 (yellow star), the Farasan Islands, the Saudi Arabian coast, and the local wadi systems (light blue lines) (Lehner and Grill, 2013). BaM; Bab al Mandab. (For interpretation of the references to colour in this figure legend, the reader is referred to the Web version of this article.)

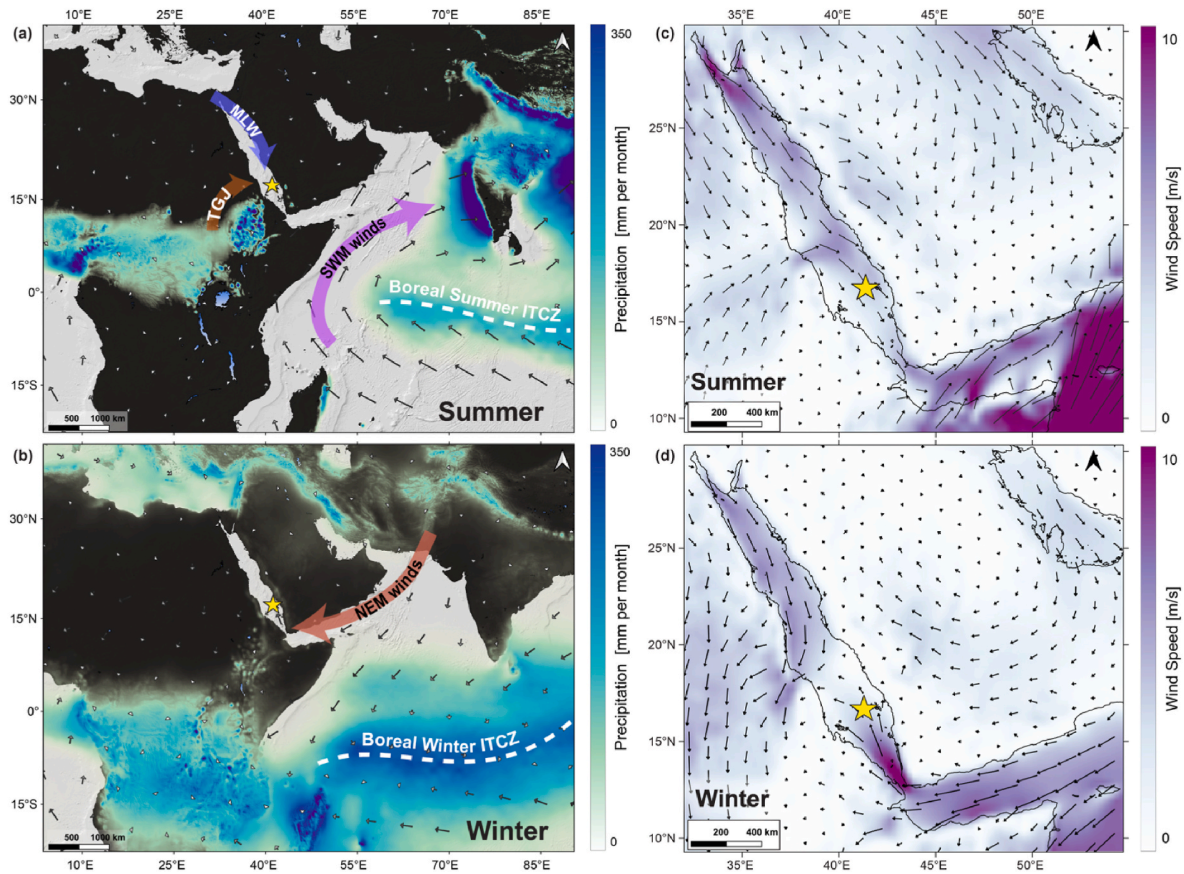

Fig. 2. Maps of regional monthly average precipitation (mm) and low-level (1000 hPa pressure level) wind vectors (m s^{-1}) for (a) boreal summer (June–August) and (b) boreal winter (December–February). Close-ups of the speed (m s^{-1}) and trajectories of the regional low-level winds (1000 hPa pressure level) for (c) boreal summer (June–August) and (d) boreal winter (December–February). Note the seasonal reversal of the wind direction. Monthly averaged precipitation data were downloaded from the CHELSA (Climatologies at High resolution for the Earth's Land Surface Areas) global downscaled dataset (Karger et al., 2017, 2021). ERA5 monthly averaged wind vectors on the 1000 hPa pressure level were downloaded from the Copernicus Climate Change Service (C3S) (Hersbach et al., 2023). Precipitation related to the African Summer monsoon (ASM) and Indian Summer monsoon (ISM) can be seen in panel (a) above Africa and west India, respectively. The yellow star marks the location of Core FA09. (a) SWM: Southwest Monsoon winds; ITCZ: Intertropical Convergence Zone; MLW: Mid-Latitude Westerlies; TGJ: Tokar Gap Jet. (b) NEM: Northeast Monsoon winds. (For interpretation of the references to colour in this figure legend, the reader is referred to the Web version of this article.)

attracted considerable attention due to the remarkable archaeological record of mid-Holocene marine sites on the Farasan Islands (Bailey et al., 2015). We focus on reconstructing the regional hydroclimatic regime while considering the profound influence sea-level has had on sedimentation. To this extent, we have generated continuous bulk geochemical and mineralogical records in order to deduce variations in the terrigenous and biogenic input. Terrigenous plant leaf-waxes are used to infer possible changes in the continental vegetation cover while the grain-size distribution and end-member modelling of the siliciclastic fraction is used to distinguish between transport mechanisms of the detrital material. The record covers the past ca. 30 kyr at an average temporal resolution of ca. 50 years. Our findings are compared to other records from the Red Sea, Gulf of Aden, and Arabian Sea in order to discern sea-level and hydroclimatic controls on a regional scale. Finally, we briefly consider the archaeological implications of our climatic and environmental findings in relation to the DISPERSE project which aimed to disentangle the relationship between geological instabilities, such as active tectonics and sea-level change, and patterns of early human dispersal (Bailey, 2015; Bailey et al., 2015).

2. Regional Setting

2.1. The Red Sea

The Red Sea is a roughly 2000 km long and 300 km wide semi-enclosed basin, situated in an arid subtropical zone in the midst of the Saharan-Arabian desert belt (Fig. 1). The sole connection to the open sea occurs in the southern section of the basin, at which the 137 m deep (Hanish sill; Werner and Lange, 1975) and 20 km wide Bab al Mandab straight facilitates water-mass exchanges with the Gulf of Aden and the Arabian Sea. Isotopic data and palaeoshoreline reconstructions suggest that although this exchange with the Gulf of Aden and Arabian Sea has been restricted at times of glacial sea-level lowstands, a continuous connection to the open sea has been maintained during at least the past 500 ka (Grant et al., 2014; Lambeck et al., 2011; Rohling et al., 2013; Siddall et al., 2003).

The basin is located between the uplifted granitoids, diorites and metamorphic rocks of the Arabian-Nubian shield (ANS); the erosional products of which end up in the Red Sea sedimentary record (e.g., Bentor, 1985; Stein et al., 2007). Where exposed, the ANS forms abrupt topographic features up to ~3000 m in elevation. Overlying the ANS are sequences of carbonates (mainly limestones and dolomites), sandstones and marls, which are interspersed with alkali basalts (Palchan et al., 2013; Stein et al., 2007; Stein and Hofmann, 1992). Situated just west and east of the ANS are two of the major dust producing regions globally; the Saharan and Arabian deserts. It is estimated that the Saharan desert produces 40–60 % of global dust emissions while the Arabian desert, which includes the Nefud Desert, Rub' al Khali and the connecting sandy formation Ad-Dahna (Fig. 1), produces around 10–20 % (Maher et al., 2010; Prospero et al., 2002).

2.2. Study site

Study site FA09 (16° 56.014′ N, 41° 07.253' E; 302 m water depth) is located on the southeastern Red Sea continental slope within the Farasan Archipelago, around 129 km off the coast of the Jizan Province in Saudi Arabia (Fig. 1). Between ~15°N and ~17°N latitude, the basin reaches its maximum width of 360 km while both continental shelves developed off the axial trough extend for more than 120 km each. The continental shelf within the Farasan Archipelago is predominantly composed of a 70–90 m deep marine terrace that shallowly dips southwestward (Sakellariou et al., 2019). This terrace is present throughout the entire Red Sea basin and is thought to have developed between 28 and 37 ka BP during the late Marine Isotope Stage (MIS) 3 (Dullo and Montaggioni, 1998). Additional submerged terraces are identified at depths of ~40 m and ~120 m, most likely corresponding to late MIS 5 (i.e., MIS 5b; 87–82 ka) and MIS 2 (29–14 ka), respectively (for more information see Sakellariou et al., 2019). The terraces, including the nearby outcropped Farasan Islands, are mostly composed of Pliocene-Pleistocene marly and reefal limestones (Almalki and Bantan, 2016, and references within). A series of shallow flat-topped sedimentary blocks (Fig. 3), separated from the main shelf predominantly due to SW–NE faulting and salt tectonics, are located east of the coring site while sub-bottom profiling reveals a thick succession (>550 m) of sedimentary deposits within this area (Sakellariou et al., 2019). On the contrary, sub-bottom profiling revealed that post glacial sedimentation on the continental shelf is practically negligible while thicker sedimentary deposits are only observed within bathymetric depressions on the main terrace (Sakellariou et al., 2019). These deposits consist of a carbonate rich, mostly fine-grained mixture of biogenic and detrital components (e.g., Basaham, 2009; Sergiou et al., 2022b).

3. Materials and methods

3.1. Core FA09

The 2.6 m long gravity Core FA09 was recovered during the 2013 R/V 'AEGAEO' DISPERSE expedition in the southern Red Sea (Bailey, 2015; Bailey et al., 2015). Macroscopic observations based on colour and textural variations divide the sedimentary record into four main lithological units (Fig. 4b) as follows (see Sergiou et al. (2022a) for a detailed lithological description and Section 4 of this paper for the age model development): Unit A: light brownish gray sandy silt from ca. 30.4 to 17.3 ka (266–144 cm); Unit B: light gray to white condensed sandy silt from ca. 17.3 to 15.4 ka (144–129 cm); Unit C: weakly laminated dark to olive brown silt from ca. 15.4 to 10.5 ka (129–84 cm), and; Unit D: light olive brown sandy silt from ca. 10.5 to 0.8 ka (84–0 cm).

3.2. X-ray fluorescence core scanning (XRF-CS)

The working half of the split core was scanned with an AVAATECH XRF core scanner at the CORELAB facility of the University of Barcelona. The scanner was equipped with an Oxford Rhodium X-ray source (4–50 kV), a Canberra X-Pips 1500-1.5 Detector with a 125 μm beryllium window and a multichannel analyzer Canberra DSA 1000 (MCA), therefore allowing the detection of elements between Al and U (Cerdà-Domènech et al., 2020). Prior to scanning, the core was smoothed and covered with a 4-μm-thick Ultralene® X-ray transmission foil in order to avoid potential contamination and desiccation of the sediment. Scanning was performed at a 2 mm spatial resolution with a 2 mm downcore and 12 mm crosscore slit size, while three replicate scans were performed every fifty measurements. Excitation configuration parameters were set at 10 kV (no filter) and 1.9 mA, with a counting time of 10 s for Al, Ca, Fe, K, Mn, Si and Ti. Moreover, Br, Rb, Sr, Zn and Zr were measured at 30 kV (Pd-thick filter) and 2 mA, with a 40 s counting time. X-ray spectra data was processed with the bAxil spectrum analysis software BrightSpec (www.brightspec.be). The reproducibility or precision of the scanning procedure was established through the

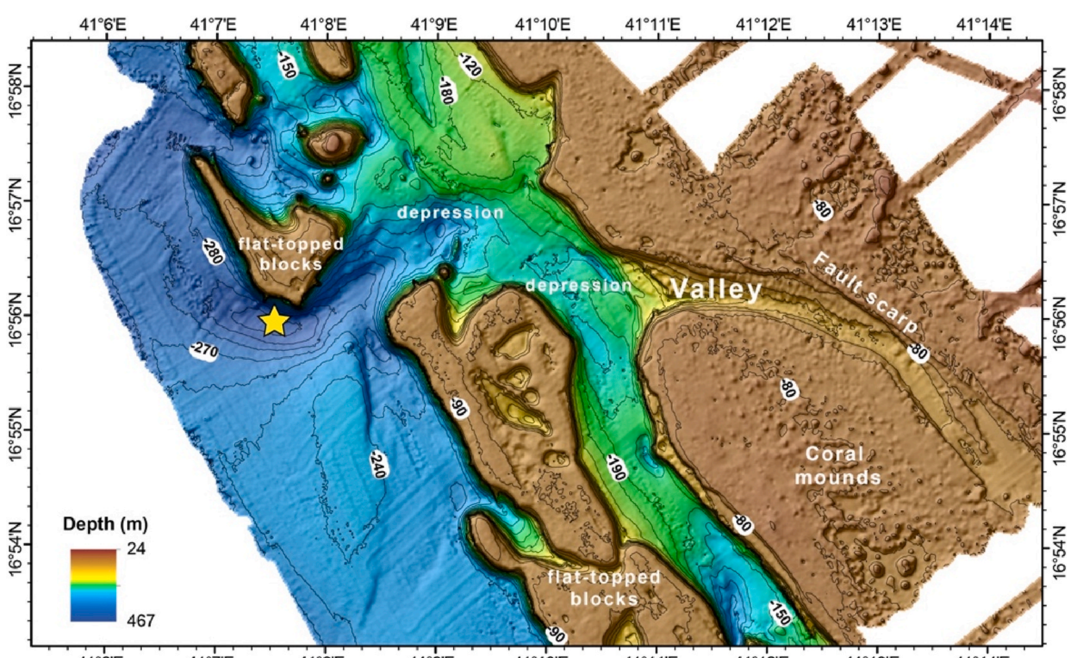

Fig. 3. Geomorphological features of the continental shelf surrounding the FA09 Core site (yellow star). Note the flat-topped blocks and the NW-SE trough (valley) situated to the east of the FA09 site (modified after Sakellariou et al., 2019). (For interpretation of the references to colour in this figure legend, the reader is referred to the Web version of this article.)

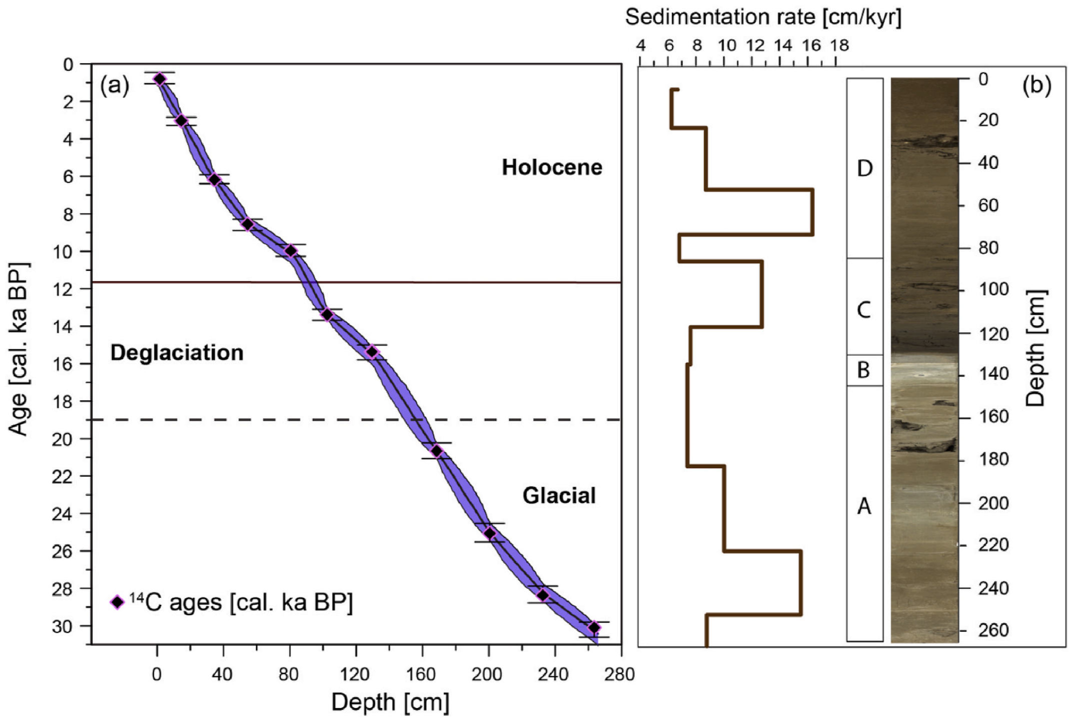

Fig. 4. (a) Bayesian age model for Core FA09. Calibrated ^{14}C ages and respective errors are illustrated through the black diamonds and error bars. The thick black line depicts the median age-depth model as calculated by the Bacon approach while gray lines show the 95 % confidence intervals. The glacial and Holocene periods are separated by a dark red line, while a dashed black line illustrates the start of the last Deglaciation at 19 ka. (b) Sedimentation rates (cm/kyr), lithostratigraphic units, and a high-resolution image of Core FA09 against depth. (For interpretation of the references to colour in this figure legend, the reader is referred to the Web version of this article.)

relative standard deviation (RSD) of the replicate measurements (for more information see Text S1). For a preliminary visualization of downcore variability and in order to counteract potential artifacts deriving from water content and sediment surface irregularities (e.g., Bertrand et al., 2024), elemental counts were normalized to the sum of all counts within each measurement.

3.3. Calibration of XRF-CS intensities

To calibrate the XRF-CS intensities and predict quantitative elemental compositions, we measured the elemental concentrations of 54 discrete bulk sediment subsamples via wavelength dispersive X-ray fluorescence (WD-XRF) and inductively coupled plasma mass-spectrometry (ICP-MS) at the Hellenic Centre for Marine Research. The calibration samples were selected according to the acquisition strategy described by Weltje et al. (2015) in order to ensure that all major compositional trends within the dataset are represented (for more information see Text S2). Major elements (Al, Ca, Fe, K, Si, Ti) were determined through a fused bead method that involved the fusion of ~600 mg of oven-dried (40 °C) ground bulk sediment with 5.5 g of lithium borate 67-33 (67 % lithium tetraborate - 33 % lithium metaborate), 0.5 g of lithium carbonate, and 0.5 g of ammonium nitrate. A few drops of lithium bromide were used as a non-wetting agent while Bunsen burners and platinum crucibles were used for the fusion. Fused beads were analysed with a Philips PW-2400 wavelength dispersive X-Ray spectrometer equipped with a Rh tube. Reference samples (U.S.G.S and National Research Council of Canada) covering a wide range of concentrations were used for instrument calibration. Expanded uncertainties (U) at a 95 % confidence interval were calculated at 5.54 % for Al, 7.10 % for Ca, 4.2 % for Fe, 12.75 % for K, 2.7 % for Si, and 4.4 % for Ti. Trace element (Mn, Sr, Zn) concentrations were determined through a microwave-assisted acid (combination of hydrofluoric acid and nitric acid) digestion method (Diegor et al., 2001) on 100 mg of oven-dried (40 °C) ground bulk sediment. A multi-element standard solution was used in order to create the calibration curve and all final solutions were analysed with a Thermo X Series II ICP-MS. Expanded uncertainties (U) at a 95 % confidence interval were calculated at 6.6 % for Mn, 9.4 % for Sr and 6.0 % for Zn.

Following elemental concentration measurement, the multivariate log-ratio calibration approach (MLC) was performed through the AvaaXelerate software in order to calibrate elemental counts and predict absolute concentrations (Weltje et al., 2015; Weltje and Tjallingii, 2008).

Linear least squares regression was performed to evaluate the strength of the XRF-CS calibration procedure, and more specifically: (i) the correlation between XRF-CS counts and the ICP-MS/WD-XRF concentrations of the calibration samples; and (ii) the correlation between the ICP-MS/WD-XRF concentrations and the MLC predicted concentrations of the calibration samples.

3.4. Grain size

Grain size distributions were determined on the acetic acid insoluble residue (IR) of 92 bulk sediment samples which have an average temporal resolution of ca. 300 years. Approximately 2 g of dry sediment was pre-treated at 60 °C for 48–72 h with 30 % hydrogen peroxide and 30 % acetic acid in order to eliminate the organic matter and carbonate fraction, respectively (modified after Sun et al., 2002). The presence of biogenic opal in the samples was considered negligible and was therefore not specifically removed, as siliceous microfossils were found to be sparse. The IR was then washed and centrifuged five times with distilled water to remove reaction products (namely calcium acetate, which is produced from the reaction of acetic acid and calcium carbonate) and any acid residue. The dry IR was then weighed in order to calculate the siliciclastic fraction (%). Grain size measurements were carried out on a Malvern Mastersizer 2000 laser particle analyzer at the Department of

Geology, University of Patras. The reproducibility of replicate measurements was over 95 %. Grain size results were classified according to Folk and Ward (1957) into the sand, silt and clay fractions.

Grain size distributions were then evaluated through end-member modelling analysis (EMMA) via the CRAN R package EMMAgeo v.0.9.7 (Dietze et al., 2012; Dietze and Dietze, 2019) in R v.4.2.2 (R Core Team, 2022). EMMA follows a grain-size distribution unmixing approach based on principal component (PCA) and factor analysis (FA) (Dietze et al., 2012; Weltje, 1997). This approach creates significant sediment subpopulations also called end-members (EM), while the optimal number of these EM is determined through goodness-of-fit tests (Dietze et al., 2012).

3.5. Mineralogy

The mineralogical composition was established on 36 samples (average temporal resolution of ca. 800 years), which were chosen based on downcore elemental variations. Approximately 5 g of wet sediment was oven-dried at 40 °C and subsequently ground with an agate pestle and mortar to obtain powder with a grain size of 1–3 μm. To improve mineral phase identification and ensure accurate quantification, all samples were spiked with an internal standard of silicon (Si) (ICSD 67788) at 5 wt% prior to x-ray diffraction (XRD) analysis. The XRD measurements were carried out at the Institute of Earth Sciences, Heidelberg University, on a Bruker D8 ADVANCE Eco diffractometer (40 kV, 25 mA) with a Cu Kα diode. The angular range of 2-theta was set between 3° and 65° and was measured with a step size of 0.02 increments (3338 steps per sample) for 0.5 s per step. Peak positions and data intensity were identified with the Diffrac.Suite EVA (Bruker Software), while quantitative phase analysis was performed with the Rietveld refinement program DIFFRAC.TOPAS (Bruker Software). Because sediment samples were not rinsed prior to analysis, potential contribution of porewater precipitates to the total halite percentage cannot be excluded. To account for this, we have also calculated the mineralogical results by normalizing the dataset without halite (see Fig. S10).

3.6. TC, TOC, TN and $CaCO_3$

The total organic carbon (TOC), total carbon (TC) and total nitrogen (TN) content was measured on ten samples in order to improve the temporal resolution of the already existing records (Sergiou et al., 2022a, 2022b). Briefly, bulk sediment samples were oven-dried at 40° and homogenized with a pestle and mortar. Approximately 10–15 mg of the sediment was transferred to silver (for TOC) and tin (for TC) capsules, while for the TOC measurements samples were consecutively treated with hydrochloric acid (2M) until all inorganic carbon was sufficiently removed. Samples were analysed on a CHN Flash Elemental Analyzer, Thermo Scientific at the Hellenic Center for Marine Research. The TOC/TN ratio was also recalculated (original ratio in Sergiou et al. (2022b)) in order to differentiate between terrestrial and marine derived organic matter (Meyers, 1994). The calcium carbonate content ($CaCO_3$; Eq. (1)) was calculated from the total inorganic carbon (TIC = TC-TOC) as follows:

$$CaCO_3\ (\%) = (TIC) \times 8.33 \tag{1}$$

3.7. Lipid biomarkers

Lipid biomarkers were measured on 20 freeze-dried and homogenized sediment samples resulting in an average temporal resolution of ca. 1500 years. Approximately 3 g of dry bulk sediment was extracted with an accelerated solvent extractor (Dionex™ ASE) and a 9:1 dichloromethane (DCM):methanol (MeOH) (v:v) mixture. The total lipid extract (TLE) was split in order to produce ~10 mg aliquots which were subsequently separated on an aminopropyl gel column (eluting solvents in brackets) into the neutral/polar (2:1 DCM:2-propanol (v:v)), free fatty acid (4 % glacial acetic acid in ethyl acetate) and phospholipid fatty acid (MeOH) fractions. The neutral/polar fraction was further separated on an alumina oxide gel column into the apolar (9:1 Hexane:DCM (v:v)), the neutral (1:1 Hexane:DCM (v:v)) and polar (1:1 DCM:MeOH (v:v)) fractions. Finally, the alkane containing apolar fraction was separated into saturated (Hexane) and unsaturated (Ethyl Acetate) hydrocarbon fractions on an Ag + silica gel column. Procedural blanks were added into all sample batches in order to track potential contamination of the analytical protocol.

The saturated *n*-alkane containing fractions were analysed on a Thermo Trace Ultra ISQ gas chromatograph (GC), equipped with a mass spectrometer (MS) and flame ionization detector (FID), fitted with a fused silica column (Agilent J&W DB-5, 30 m length, 0.25 mm ID, 0.25 μm film thickness). Hydrogen was used as the carrier gas and samples were injected in splitless mode. The oven temperature was held at 60 °C for 1 min, then ramped from 60 °C to 320 °C at a rate of 6 °C/min followed by a 12-min isothermal. *n*-Alkanes were identified according to their retention times and characteristic mass spectra fragmentation patterns while quantification was performed through an external 5α-androstane calibration curve. *n*-Alkane concentrations were normalized to the TLE and reported in ng/g TLE. Sample preparation and measurement was performed at the Department of Civil and Environmental Engineering and Earth Sciences, University of Notre Dame.

To assess the variability of allochthonous terrigenous material input at our study site, we calculated the sum abundance and average chain length (ACL; Eq. (2)) of the odd, long-chain *n*-alkane (C_{27}–C_{35}) homologues; commonly synthesized by higher terrestrial plants (Eglinton and Hamilton, 1967). The carbon preference index (CPI; Eq. (3)) was calculated in order to assess the degree of *n*-alkane degradation (Marzi et al., 1993).

$$ACL = \Sigma(Cn \times n) / \Sigma(Cn) \tag{2}$$

$$CPI = (\Sigma odd\ (C_{21\text{-}33}) + \Sigma odd\ (C_{23\text{-}35}))\ /\ (2\Sigma even(C_{22\text{-}34})) \tag{3}$$

3.8. Mass accumulation rates (MARs)

Mass accumulation rates (also referred to as fluxes throughout this text) were calculated for the siliciclastic (detrital), total organic carbon (TOC), and calcium carbonate ($CaCO_3$) fractions of the sediment record. Mass accumulation rates (MAR; Eq. (4)) were calculated as follows:

$$MAR\ (g.cm^{-2}.kyr^{-1}) = SR \times DBD \times [X\ \%] \qquad [4]$$

Where SR is the sedimentation rate (cm.kyr^{-1}) calculated according to the Bayesian age model and DBD (g.cm^{-3}) is the dry bulk density and [X %] is the concentration of each component. Dry bulk density values were taken from Sergiou et al. (2022a).

3.9. Clustering and Principal Component Analysis

To identify the dominant factors controlling temporal proxy variability and sedimentation processes we conducted k-means clustering and a Principal Component Analysis (PCA) on selected proxies from our mineralogical (%) (aragonite, calcite, Mg-calcite, dolomite, illite, quartz), end-member analysis (EM1, EM2, EM3, EM4), MLC calibrated and normalized XRF-CS (for Br, Rb, Zr) elemental composition (Al, Br, Ca, Fe, K, Mn, Rb, Si, Sr, Ti, Zr), and TOC (%), CaCO3 (%) datasets. Prior to statistical treatment and due to significant discrepancies in sample resolution all missing values were imputed through linear interpolation. The interpolated datasets were subjected to k-means clustering while the optimal number of clusters was chosen based on the Calinski-Harabasz criterion (Caliñski and Harabasz, 1974). Finally, the PCA was applied to centered and normalized values. K-means clustering and PCA were both performed in R v.4.2.2 (R Core Team, 2022) through the packages readxl, fpc, factoextra, ggplot2, tibble, dplyr, reshape2, ggbiplot, corrplot, FactoMineR.

4. Age model development

In order to develop the age model for FA09, eleven accelerator mass spectrometry (AMS) ^{14}C ages were measured on both planktic and benthic foraminifera tests. The initial five measurements were performed on ~10 mg of planktic foraminifera tests (*Globigerinoides ruber*) at the Scottish Universities Environmental Research Centre (SUERC) and have already been published (Sergiou et al., 2022a) (Table 1). Here we have added another six AMS ^{14}C ages (Table 1) in order to improve dating accuracy within the Holocene and the Last Glacial Maximum (LGM) periods. For the new AMS ^{14}C ages, five samples of ~5–10 mg of planktic foraminifera tests (*G. ruber* and *G. sacculifer)* and one sample of ~5 mg of benthic foraminifera tests (*Anomalinoides* sp. and *Hanzawaia* sp.) were analysed at the LARA laboratory of the University of Bern. The age model was developed through Bayesian age-modelling, which was performed with the CRAN R package rbacon (v.3.0.0) (Blaauw and Christen, 2011) (Fig. 4a). All eleven ^{14}C ages were calibrated within rbacon considering the nearest available reservoir effect of $\Delta R = -59 \pm 38$ years (Southon et al., 2002), which has been previously used for Core FA09 (Sergiou et al., 2022a, 2022b). We must note that variations in sea level and circulation regimes within the Red Sea have likely affected residence times and, consequently, reservoir ages (Biton et al., 2008; Bouilloux et al., 2013b; Rohling et al., 2008; Siddall et al., 2004; Trommer et al., 2010), although we lack sufficient evidence to constrain this effect throughout the record. With this in mind, we acknowledge the potential limitations of our age model when interpreting millennial-scale events. Sedimentation rates exhibit relative stability across the entire record maintaining values between approximately 6 and 9 cm/kyr (Fig. 4b). Three notable exceptions are observed within the ca. 30–28.4 kyr, ca. 15.3–13.3 kyr, and ca. 9.9–8.5 kyr intervals during which sedimentation rates increase up to ca. 19 cm/kyr (Fig. 4b).

The refined age model suggests that Core FA09 spans from ca. 30.4 to ca. 0.8 ka. For the chronostratigraphic interpretation of our record and the references for each period please see Text S3. To facilitate the comparison of our data with other available regional records, we have recalibrated the age models of Cores MD8 (Bouilloux et al., 2013b), MD2 (Bouilloux et al., 2013a) and GeoB5844-2 (Arz et al., 2003) using the same approach as for Core FA09. Specifically, their age models were redeveloped through Bayesian age modelling using the MARINE20 calibration curve (Heaton et al., 2020), and reservoir effects of $\Delta R = 64 \pm 68$ years (Southon et al., 2002) for Cores MD8 and MD2, and $\Delta R = -86 \pm 40$ years (Siani et al., 2000) for Core GeoB5844-2 were applied.

5. Results

5.1. Calibration and quantification of the XRF-CS measurements

The statistical evaluation of the XRF-CS counts and the calibration sample concentrations reveals strong correlations for Fe ($R^2 = 0.81$), Zn ($R^2 = 0.78$), K ($R^2 = 0.75$) and Ti ($R^2 = 0.70$) (Fig. S1). Moderate correlations are observed for Sr ($R^2 = 0.47$), Mn ($R^2 = 0.45$), Si ($R^2 = 0.39$), and Ca ($R^2 = 0.26$), and weak correlation for Al ($R^2 = 0.19$) (Fig. S1). Assessment of the MLC approach through the correlation of predicted and measured concentrations of the calibration samples reveals a significantly improved relationship for Fe ($R^2 = 0.96$), K ($R^2 = 0.96$), Ti ($R^2 = 0.96$), Si ($R^2 = 0.90$), Al ($R^2 = 0.84$), Ca ($R^2 = 0.80$), and Zn ($R^2 = 0.71$), and a moderate one for Mn ($R^2 = 0.57$) and Sr ($R^2 = 0.41$) (Fig. S2). Downcore comparisons of XRF-CS counts, calibration sample concentrations and MLC predicted concentrations reveal discrepancies between counts and concentrations for Al, Ca, K, Si, and Ti throughout the length of the core, with the most significant discrepancies occurring from ca. 15.4 to 14.6 ka (Fig. S4). For more information concerning the sources of uncertainty related to the XRF-CS elemental intensities and the MLC calibration approach the reader is referred to Text S4, Figure S8 and Figure S9.

5.2. Elemental composition

The MLC predicted elemental concentrations of Al, Fe, K, Mn, Si, Ti, Zn (Fig. S3) and the normalized (element counts/total counts) XRF-CS counts of Rb and Zr (Fig. S5) exhibit similar trends, which are characterized by a pronounced shift at 14.6 ka. Specifically, high concentrations for these elements are observed between ca. 30 and 14.6 ka, followed by low concentrations from 14.6 onwards. Superimposed on this long-term trend are numerous abrupt short-term fluctuations, particularly between ca. 30 and 14.6 ka, whereas a steadily increasing trend is observed for Fe, K, Mn, Rb, Si, Ti, and Zr from ca. 5 ka onwards (Figs. S3 and S5). Anti-correlated with the abovementioned elements, Ca values are low between ca. 30 and 14.6 ka and high between ca. 14.6 and 0.8 ka (Fig. S3). Fluctuations between ca. 30 and 14.6 ka are of low amplitude, while a rather steady decrease in concentrations is observed from ca. 5 ka onwards. The downcore variation of Sr is unlike all other elements, exhibiting a significant increase from ca. 12 to 10 ka. Normalized XRF-CS Br counts (Fig. S5) also differ from the other elemental trends and exhibit high values between ca. 16 and 11 ka.

To gain a better understanding of the sedimentation processes governing the southern Red Sea, we utilize the Ti/Ca ratio of the MLC predicted elemental concentrations (for more information concerning the MLC calibration see Text S4) as a tracer of detrital versus marine sedimentation. This ratio has been previously used in several marine records (e.g., Croudace and Rothwell, 2015; Hodell et al., 2015, 2013; Koutsodendris et al., 2021) and has also been used as a dust input proxy

Table 1
Calibrated AMS^{14}C ages obtained on planktic and benthic (marked with an asterisk) foraminifera tests using the calibration curve MARINE20 (Heaton et al., 2020) and considering a reservoir effect of $\Delta R = -59 \pm 38$ years.

Lab Code	Core depth (cm)	^{14}C Age (yr BP)	Calibrated Age Range (2σ) (cal yr BP)	Calibrated Median Age Probability (cal yr BP)	Remarks
SUERC-70198	1.5	1515 ± 32	451–1052	803	Sergiou et al. (2022a)
BE-20368.1.1	14.5	3255 ± 31	285–3283	3031	This study
SUERC-70199	34.5	5916 ± 32	5916–6391	6172	Sergiou et al. (2022a)
BE-20369.1.1	54.5	8173 ± 38	8286–8885	8555	This study
SUERC-70200	80.5	9252 ± 32	9644–10270	9975	Sergiou et al. (2022a)
BE-20370.1.1	102.5	12001 ± 40	13091–13681	13379	This study
SUERC-70201	129.5	13366 ± 56	15006–15789	15368	Sergiou et al. (2022a)
BE-20371.1.1	168.5 *	17810 ± 58	20227–21074	20662	This study
BE-20372.1.1	200.5	21664 ± 89	24527–25523	25062	This study
BE-20373.1.1	232.5	25017 ± 99	27874–28767	28373	This study
SUERC-70202	263.5	26655 ± 86	29801–30602	30097	Sergiou et al. (2022a)

in the central Red Sea (Roberts et al., 2011). According to the PCA results, the Ti/Ca ratio is strongly correlated to the first principal component (PC1) (Fig. 9i and j), and it is therefore best suited to represent the compositional variation of our record. Moreover, we prefer the use of the Ti/Ca ratio rather than the Fe/Ca ratio, despite the high Fe content in the FA09 record, as it is insensitive to potential redox fluctuation effects which tend to be pronounced in the Red Sea due to shifts in oxygenation levels observed over millennial timescales (e.g., Almogi-Labin et al., 1991; Fenton et al., 2000). Given the clear correlation between Br and TOC, we use the logarithmic Br/Ti ratio (Fig. 9c), to track high-resolution changes of the organic matter content, similarly to Ziegler et al. (2008). However, since the Br counts have not been calibrated we use this ratio with caution and only as a supplementary indicator which is supported by the more robust TOC values.

5.3. N–alkane abundances and distributions

n-Alkane (C_{16}-C_{35}) concentrations range between 19113 and 415400 ng.g^{-1} TLE (sum of $C_{16\text{-}35}$), while the terrestrial, long-chain *n*-alkanes (C_{27}, C_{29}, C_{31}, C_{33}) dominate the record. The sum of the terrestrial long-chain odd alkanes ranges between 5160 and 144890 ng. g^{-1} TLE. Both the concentrations of the total *n*-alkanes ($\Sigma[C_{16\text{-}35}]$) (Fig. 5a) and the sum of the long-chain terrestrial *n*-alkanes (Σodd[$C_{27\text{-}35}$]) (Fig. 5b), show a decreasing trend between ca. 30 and 16 ka, which is followed by an increase from ca. 16 to 8 ka, while from ca. 8 ka onwards values decrease once again. ACL values range between 29.5 and 31.3 while the average of value of 30.2 increases to 31.2 during the period between ca. 16 and 9 ka (Fig. 5c). The CPI ranges between 1 and 3.2, indicating a predominance of well-preserved plant-waxes (Marzi et al., 1993) (Fig. 5d).

5.4. Mineralogical composition

The bulk mineralogical record is dominated by the carbonate fraction (47–80 %), which includes calcite (7–29 %), magnesian calcite (11–38 %), aragonite (10–35 %), and, to a lesser extent, dolomite (0.5–4.2 %) (Fig. S6). Aragonite values are relatively low (average 16 %) from ca. 30 to 14.6 ka, while an abrupt increase at ca. 14.6 ka leads to average values of 28 % between ca. 14.6 and 0.8 ka. Magnesian calcite, which seems to mirror the trend observed in aragonite, remains relatively stable at 19 % between ca. 30 and 14.6 ka although a gradual decline is observed between ca. 19 and 14.6 ka. This decline is followed by an abrupt increase at ca. 14.6 ka, similar to the one observed in aragonite. Pronounced fluctuations are observed for calcite (values ranging from 8 to 20 %) between ca. 19 and 8 ka. Quartz (0.3–13.5 %) and illite (0.9–14.5 %) represent a minor fraction of the bulk mineralogy (Fig. S6). Both minerals show higher concentrations between 30 and 14.6 ka, followed by an abrupt decrease at ca. 14.6 ka. Between ca. 10 and 8 ka, quartz values show a small increase of about 1 %, while illite shows an increase of around 4 % between ca. 10 and 5 ka. At ca. 2.8 ka both quartz and illite exhibit an abrupt peak which coincides with a carbonate decrease of similar amplitude. However, since this peak is only observed in one sample, interpretation should be approached with caution. Minor contributions of actinolite, albite, clinochlore, and orthoclase are observed throughout the record (Fig. S6). Gypsum (0–10 %) is observed in a few samples, while celestine (one sample at 12.8 %) is found at 11.3 ka (Fig. S6). Halite (3–10 %) is present throughout the record, although there is a clear decrease of values from ca. 15 ka onwards (Fig. S6).

5.5. Grain sizes and end-member modelling of the siliciclastic fraction

The siliciclastic fraction exhibits a generally decreasing trend throughout the record, with concentrations from around 33 % at 30 ka, to 17 % at 0.8 ka (Fig. 6a). According to the XRD results, siliciclastic minerals include actinolite, albite, clinochlore, illite, orthoclase, and quartz (Fig. S6). A minor presence of authigenic celestine, authigenic quartz and authigenic clinochlore could potentially be included in the siliciclastic fraction (Fig. S6). The overall grain size composition is poorly sorted, and dominated by the silt (4–63 μm) fraction (60–77 % of the total composition) (Fig. 6d). Higher sand (>63 μm) contents are observed from ca. 30 to 14.6 ka (Fig. 6e) while clay (<4 μm) contents increase between ca. 14.6 and 0.8 ka (Fig. 6c). To better explain grain-size variability we opted for a four end-member (EM) model which accounts for 70 % of the total variance (Figure S7 and Fig. 7a). We consider this model as the optimal solution based on a balance between total

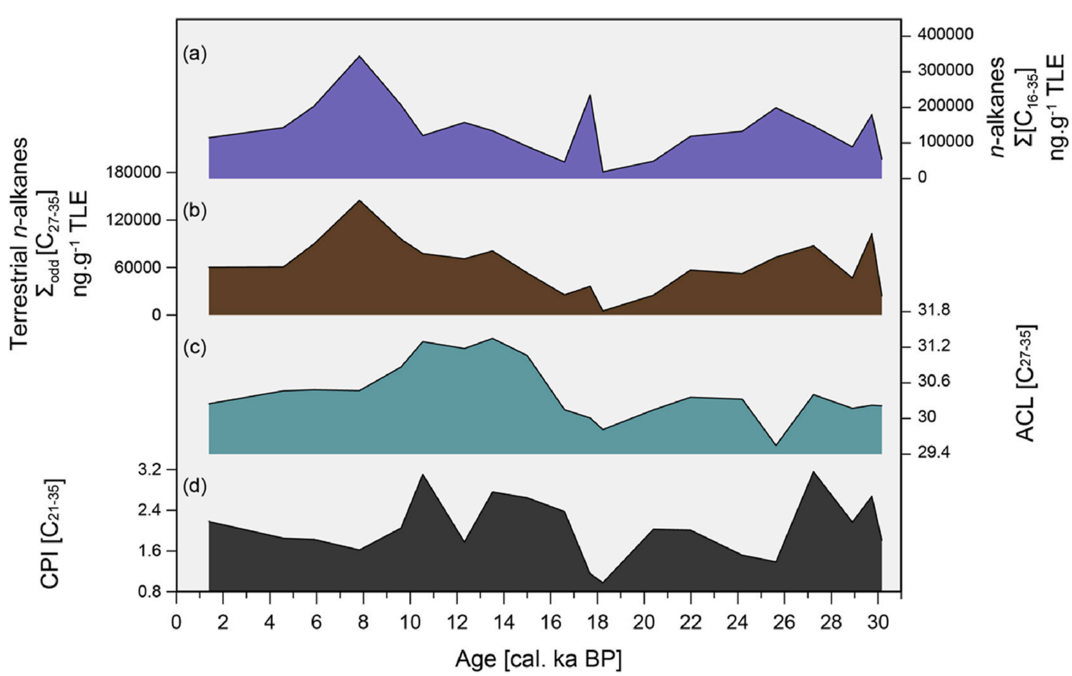

Fig. 5. *n*-Alkane results for Core FA09 including, (a) The sum of the total *n*-alkanes $C_{16\text{-}35}$ (ng.g^{-1} TLE), (b) The sum of the (terrestrial) odd long-chain *n*-alkanes $C_{27\text{-}35}$ (ng.g^{-1} TLE), (c) the average chain length (ACL) index of the odd long-chain $C_{27\text{-}35}$ *n*-alkanes, and, (d) the carbon preference index (CPI) of the $C_{21\text{-}35}$ *n*-alkanes.

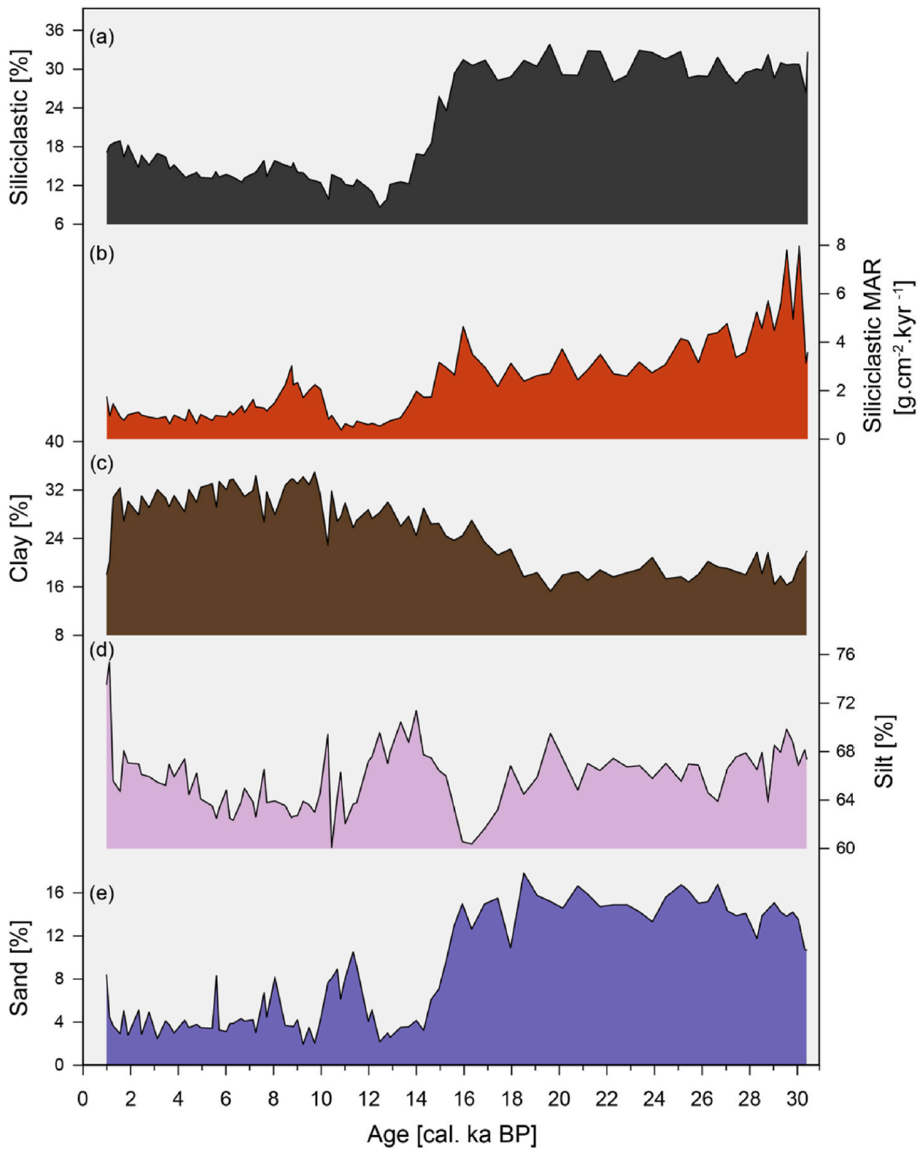

Fig. 6. The siliciclastic fraction of Core FA09 including, (a) siliciclastic percentages (%), (b) siliciclastic mass accumulation rates (MAR) (g.cm^{-2}.kyr^{-1}), (c) clay (%), (d) silt (%), and, (e) sand (%) percentages.

explained variance and interpretability. The use of fewer than 4 EMs does not seem to adequately capture the variability of the finer fraction, whereas the addition of more EMs would only slightly increase the explained variance (up to ~72 %) but reduce the ability to assign meaningful interpretations to each EM (for more information see Fig. S7). The relative contributions of the four end-members are 16.5 % for EM1, 29.4 % for EM2, 48.6 % for EM3 and 5.4 % for EM4. The major modes for each EM are at 0.8 μm for EM1, 10 μm for EM2, 52 μm for EM3, and 79 μm for EM4. Coarse-grained EM4 and EM3 dominate the record between ca. 30 and 14.6 ka, while the finer-grained EM2 dominates from ca. 14.6 to 0.8 ka (Fig. 7b). The fine clay EM1 is present throughout the record, although a substantial increase is observed from ca. 18 ka onwards, reaching a peak between ca. 10 and 6 ka.

5.6. Siliciclastic, TOC, and $CaCO_3$ mass accumulation rates (MARs)

Siliciclastic MARs range from 0.4 to 8 g.cm^{-2}.kyr^{-1} and exhibit a generally decreasing trend throughout the record (Fig. 6b). Three distinct increases occur between ca. 30 and 28 ka, ca. 17 and 15 ka, and finally, ca. 10 and 8 ka. TOC MARs range from 0.04 to 0.35 g.cm^{-2}.kyr^{-1} and show two pronounced increases from ca. 16 to 12 ka and from ca. 10 to 8 ka (Fig. 9a). $CaCO^3$ MARs range from 3.2 to 16.1 g.cm^{-2}.kyr^{-1} and present three peaks from ca. 30 to 28 ka, from ca. 16 to 13 ka, and from ca. 10 to 8 ka (Fig. 9h).

5.7. Multivariate statistical analysis

K-means clustering defined two main lithostratigraphic units within the record (Fig. 8a). The first unit corresponds to the period from ca. 30 to 14.4 ka, and the second covers the period from ca. 14.4 to 0.8 ka. PCA reduced the dimensionality of our selected proxy dataset by identifying two principal components (PCs), which account for 79.4 % of the total data matrix variance (Fig. 8b). The first principal component (PC1) explains 69.2 % of the total variance, whereas the subsequent PC2 explains 10.2 % and will therefore not be discussed further. PC1 shows a bipolar distribution, highlighting two distinct groups amongst the investigated parameters. Positive loadings for grain-size EM3, EM4, Al, Br, Fe, K, Mn, Si, Ti, Zr, Rb, illite, quartz and dolomite are predominant between ca. 30 and 14.4 ka (Fig. 8c). In contrast, negative loadings for grain-size EM1, EM2, Ca, Sr, $CaCO_3$, TOC, aragonite, Mg-calcite and calcite dominate from ca. 14.4 to 0.8 ka (Fig. 8c).

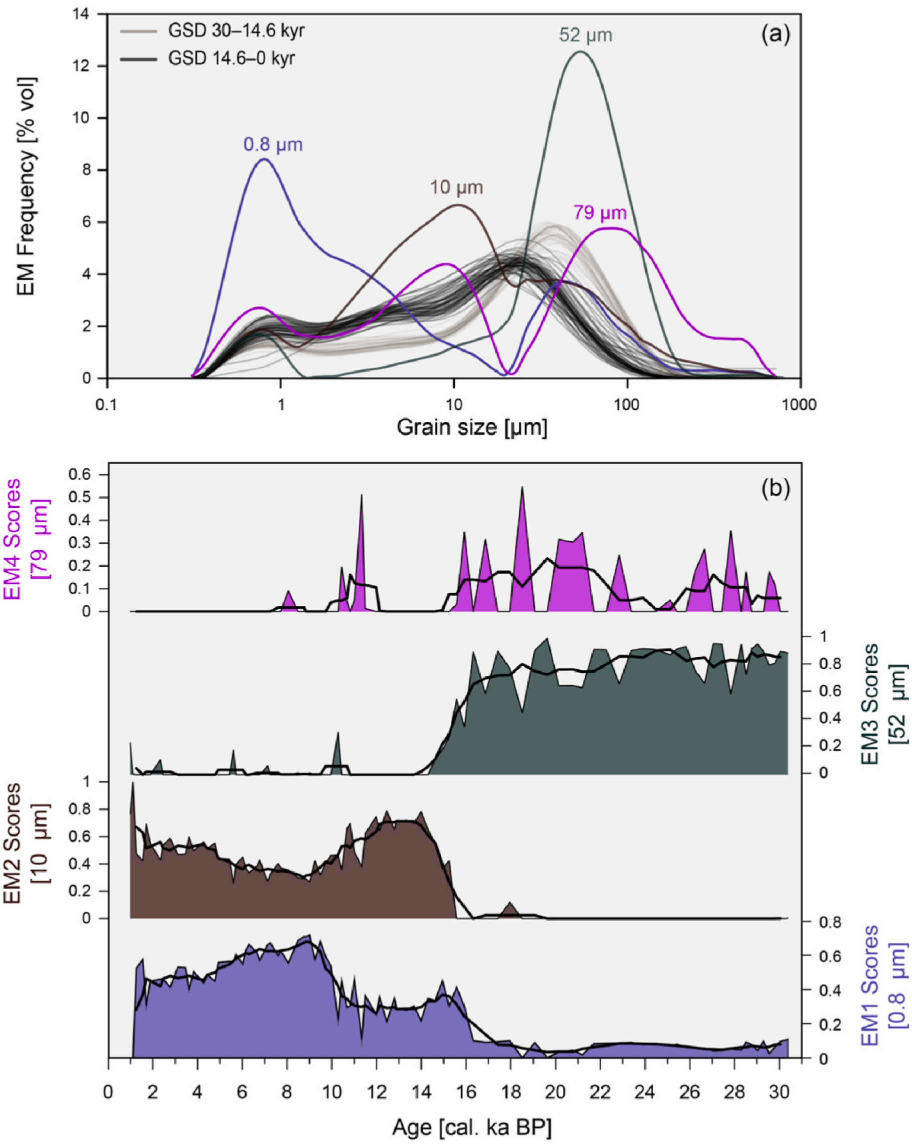

Fig. 7. End-member modelling analysis (EMMA) results of the siliciclastic grain-size distributions (GSDs) for Core FA09. (a) GSDs of all individual samples (shades of gray) overlain by the GSDs of EM 1 (0.8 μm), EM 2 (10 μm), EM 3 (52 μm), and EM 4 (79 μm). The 4 end-members explain 70 % of the total data variance. (b) Downcore relative contributions (scores) of EM 1, EM 2, EM 3, and EM 4 with the respective running averages (black lines). EM scores represent the proportion of variance explained by the respective EM at the specific ages. (For interpretation of the references to colour in this figure legend, the reader is referred to the Web version of this article.)

6. Discussion

6.1. Sedimentary composition and transport pathways in the southern Red Sea

The integrated evaluation of lithological, geochemical, and mineralogical proxies from the FA09 record delineates two distinct phases of sedimentation during the past 30 kyrs. Statistical evaluation through k-means clustering and PCA reveals two compositionally distinct clusters, which correspond to detrital-dominated (Cluster 1) and marine-dominated (Cluster 2) phases (Fig. 8a and b). These clusters are temporally aligned with increased terrigenous sedimentation from 30 to 14.6 ka (Cluster 1) and marine sedimentation from 14.6 to 0.8 ka (Cluster 2). However, since sedimentary records are inherently subject to closed-sum constraints, caution must be taken when interpretating variations of the terrigenous and biogenic components. To mitigate these closed-sum effects, mass accumulation rates are also discussed throughout the text in order to provide a more robust measure of sedimentary input dynamics.

In the Red Sea, the siliciclastic fraction primarily represents terrigenous detritus with distinctive volcanic and granitic components (Palchan et al., 2013, 2018; Rojas et al., 2019; Stein et al., 2007). Some minor authigenic mineral precipitation in the form of illite-smectite mixed layer clays, chlorites and Fe-rich silicates has also been reported (e.g., Stein et al., 2007). According to the positive loadings of PC1 (Fig. 8c), elements such as Al, Fe, K, Rb, Si, Ti, and Zr are strongly correlated to each other and are indicative of both fine terrigenous clay (Al, Fe, Si, Rb, K) and of coarser silt and sand fractions (Si, Ti, Fe, Zr) (e.g., Basaham, 2009; Mulitza et al., 2008; Sirocko et al., 2000). PC1 also exhibits a strong correlation between the abovementioned elements and quartz and illite (Fig. 8b and c); detrital minerals and their weathering products that derive from the erosion of non-alkaline granitoids and metamorphic formations of the Arabian-Nubian shield (ANS) and the uplifted terrains surrounding the Red Sea basin (Sirocko and Lange, 1991).

End-members EM3 (52 μm) and EM4 (79 μm) of the siliciclastic

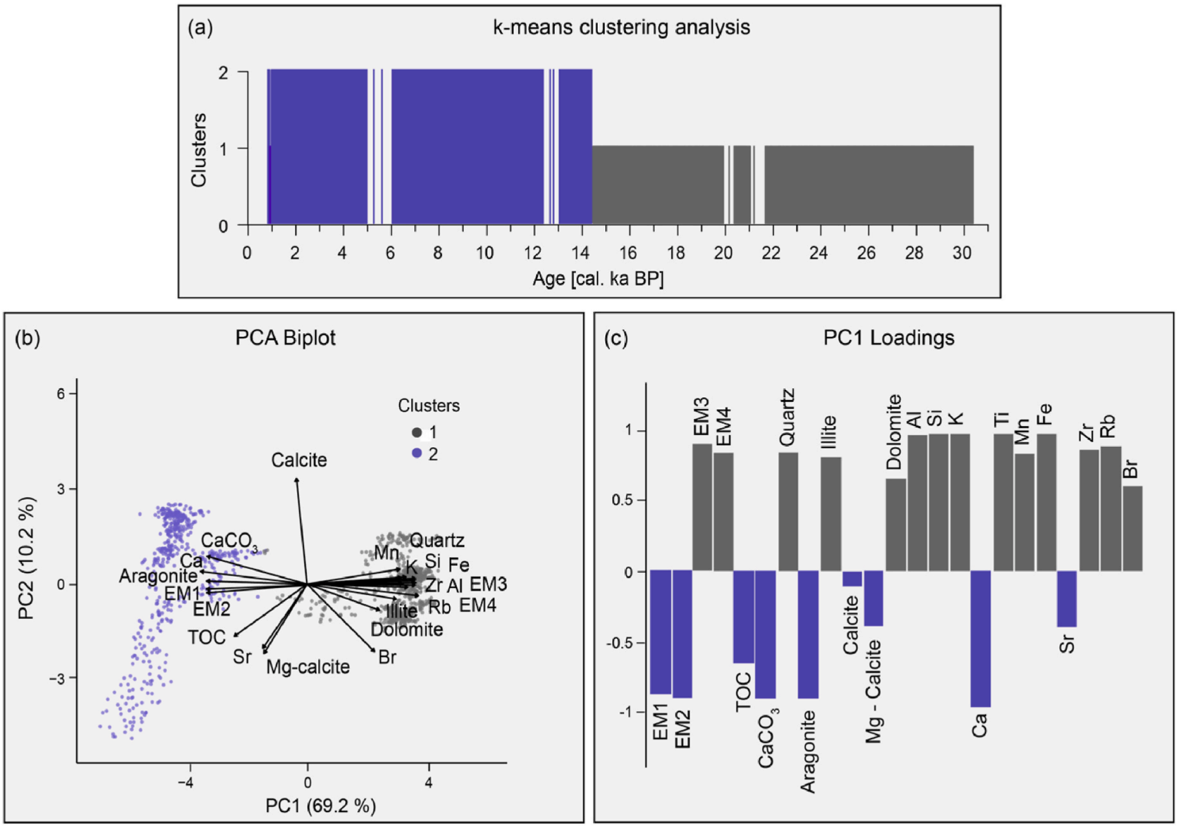

Fig. 8. Multivariate statistical analysis results for Core FA09. (a) A timeseries of the two clusters produced from the k-means clustering analysis. Gaps are due to the absence of the XRF-CS data for the respective intervals. (b) PCA biplot with PC1, PC2 and the two clusters, and (c) PC1 loadings.

fraction (Fig. 7a and b) represent coarse grains that require higher transport energy and/or originate from proximal sediment sources. Previous studies within the Red Sea and Gulf of Aden have utilised grain-sizes as indicators of transport pathways, revealing a strong association between coarser grain-sizes and increased wind intensity during the glacial period (Clemens and Prell, 1990; Ehrmann et al., 2024; Palchan et al., 2013; Rojas et al., 2019). In agreement with this, EM3 (52 μm) aligns with a coarser aeolian mode, centered around 50 μm, previously identified in the southern Red Sea (Rojas et al., 2019). Regional precipitation is presumed to be limited during this time (e.g., Fleitmann et al., 2011; Tierney et al., 2017), thereby inhibiting the intense activation of any local runoff. We therefore interpret both these end-members to primarily reflect an aeolian transport pathway throughout the glacial, while our findings corroborate the above-mentioned global trend of higher glacial dust loads reflecting increased aridity, reduced vegetation cover, and stronger wind systems (Lambert et al., 2008; Larrasoaña et al., 2003; McGee et al., 2010; Roberts et al., 2011).

At ca. 14.6 ka, a rather abrupt transition towards the marine-dominated cluster 2 (Fig. 8a) indicates a significant shift in the sedimentation regime of the southern Red Sea. The negative loadings of PC1 show a strong correlation between $CaCO_3$, TOC, and elements such as Ca and Sr (Fig. 8c). This group is primarily associated with marine productivity, given that Ca is largely related to biogenic sources such as foraminifera and coccolithophore shells. In marginal environments like the Red Sea basin, however, we cannot exclude the input of detrital Ca following the weathering of both the surrounding Ca-containing minerals such as feldspar and plagioclase (Rebolledo et al., 2008) and of the exposed reefal limestone platforms which form the Farasan Islands (Basaham, 2009; Pavlopoulos et al., 2018). Similarly, Sr is incorporated by calcifying organisms simultaneously with Ca but is preferentially fixed in aragonite (e.g., Finch and Allison, 2007; Sunagawa et al., 2007).

The abovementioned marine-related elements correlate well with aragonite, Mg-calcite and to a lesser extent calcite; carbonate minerals that are both chemically and biochemically precipitated and have been found to be well preserved in the central Red Sea (Almogi-Labin et al., 1998). In the case of aragonite, primary sources are considered to be pelagic pteropods and needle-shaped aggregates from green algae or other biotic/abiotic precipitates (Böning and Bard, 2009; Milliman, 1974; Milliman et al., 1969). These minerals are major constituents of the bulk mineralogical composition of our record and have also been abundantly found in the sediments of the Jizan shelf, east of our study area (Abou-Ouf and Elshater, 1992).

End-members EM1 (0.8 μm) and EM2 (10 μm), which dominate the sedimentary composition from 14.6 ka onwards, reflect fine siliciclastic components, which we here consider to be of both fluvial and aeolian origin (Fig. 7a and b). We interpret the very fine clay EM1 (0.8 μm) to be primarily associated with fluvial suspension, consistent with previous studies from the central Red Sea that have linked the fining of the detrital fraction to episodic fluvial activity during periods of increased precipitation (Ehrmann et al., 2024; Palchan et al., 2013; Palchan and Torfstein, 2019). While no major riverine systems drain within the southern Red Sea, multiple smaller wadi systems along the Saudi Arabian coast (e.g., Alharbi et al., 2016) may have contributed a fluvial component to our core site during these wet periods. Additionally, it is plausible that a small fraction of fine detrital material was transported from the Baraka Wadi (Fig. 1) to our site via wind-generated wave activity, which is most prevalent during the summer months (e.g., Langodan et al., 2018). The Baraka Wadi is the largest contributing riverine system in the Red Sea region and is seasonally active for approximately 40–70 days per year, primarily during autumn, with an annual discharge ranging from 200 to 970 × 10^6 m^3 of water (Trommer et al., 2011). The fine silt-sized EM2 (10 μm) likely represents finer detrital aeolian input, transported either over larger distances or by weaker wind systems. This

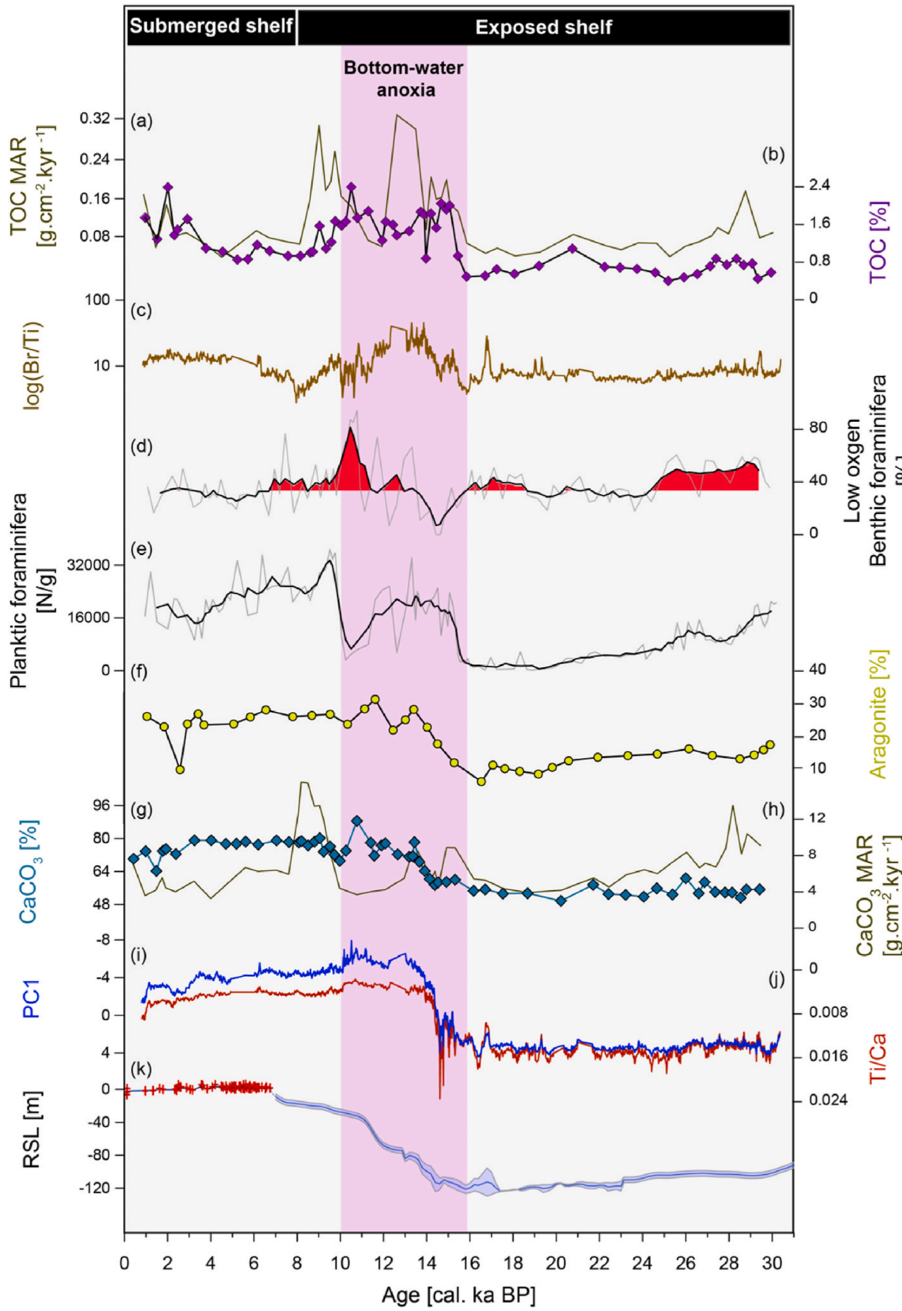

Fig. 9. Sea-level controls on the on the southern Red Sea sedimentation. All proxy records are from Core FA09. (a) Total organic carbon (TOC) mass accumulation rates (MAR) (g.cm^{-2}.kyr^{-1}) (this study), (b) TOC concentrations (%) (Sergiou et al. (2022b), and this study), (c) XRF-CS log(Br/Ti) (this study), (d) low-oxygen benthic foraminifera assemblages (%) (Sergiou et al. (2022b), (e) planktic foraminifera (N/g) (Sergiou et al., 2022a), (f) aragonite concentrations (%) (this study), (g) calcium carbonate ($CaCO_3$) concentrations (%) (Sergiou et al. (2022b), and this study), (h) $CaCO_3$ mass accumulation rates (MAR) (g.cm^{-2}.kyr^{-1}) (this study), (i) first principal component (PC1) (this study), (j) Ti/Ca MLC predicted ratio (this study), (k) Red Sea Relative Sea Level (RSL) reconstruction, synthesized by combined data from Al-Mikhlafi et al. (2021) (red crosses), Arz et al. (2007), and Grant et al. (2012). The shaded pink area marks an interval of high surface productivity and bottom-water anoxia between ca. 15.4 ka and 10 ka. (For interpretation of the references to colour in this figure legend, the reader is referred to the Web version of this article.)

interpretation seems to be consistent with previous studies from the southern Red Sea and Gulf of Aden that document an increase in a fine aeolian end-member (15 μm) during the Holocene (Rojas et al., 2019). A fine dust end-member is also present in the central Red Sea (Core KL11) (Ehrmann et al., 2024); however, this end-member appears coarser, with modal peaks at 20 μm and 40 μm, potentially indicating more proximal dust sources compared to those reaching the FA09 site. Distinguishing the processes behind the finer end-members (EM1 and EM2) remains challenging due to their similar grain size characteristics and potential for mixed transport. Consequently, the influence of a slightly coarser fluvial component from nearby wadis cannot be ruled out in interpretations of EM2. In any case, the dominance of coarse and fine dust end-members (relative contributions of >80 %) throughout the entire FA09 record suggests that aeolian dust transport is the primary sediment transport mechanism in the southern Red Sea.

6.2. Sea level related imprints on sedimentation

Accounting for 69 % of the total compositional variability in our record, PC1 exhibits a notable similarity to the Red Sea relative sea-level curve (Fig. 9i–k). This resemblance underscores the long-term control of sea level on the southern Red Sea sedimentation and is in agreement with previous studies that have also reported the strong impact of sea-level on the Red Sea geochemical records (e.g., Bouilloux et al., 2013b; Sergiou et al., 2022a; Siddall et al., 2004, 2003).

Combined Red Sea Relative Sea Level (RSL) reconstructions (Al-Mikhlafi et al. (2021), Arz et al. (2007) and Grant et al. (2012); Fig. 9k) indicate that the RSL remained substantially low during the Last Glacial Maximum (LGM) (26.5–19 kyr), reaching up to 125 m below the present level. With the onset of the last Deglaciation (19–11.7 kyr), sea level was marked by short term fluctuations of up to ca. 10 m that persisted until ca. 14.6 ka (Clark et al., 2004) (Fig. 9k). This period was followed by a rapid sea-level rise, of ca. 90 m in total, which continued until the early Holocene, at ca. 11 ka, after which rates decreased until the eventual stabilisation at present levels at ca. 7 ka (Fig. 9k).

The impact of deglacial sea-level rise on sedimentation could in theory be partially controlled by the geomorphological configuration of the broad (over 120 km wide) and shallow (70–90 m deep) continental shelf extending east of our study area. During the LGM sea-level low-stand, shelf exposure significantly shortened the distance between the FA09 site and the shoreline, reducing it from around 129 km (present shoreline) to just a few kilometers (LGM palaeoshoreline; Sakellariou et al., 2019) (Fig. 10a). As a result, the FA09 site was positioned in close proximity to the exposed shelf, which may have served as an additional proximal source of detrital material. The rapid deglacial sea-level rise at ca. 14.6 ka could have led to the sudden flooding of large shelf areas around our site potentially removing or decreasing this source of detrital input and thus altering sedimentation dynamics at the FA09 site. Notably, according to our PCA results an abrupt shift in sedimentation occurs at ca. 14.6 ka (Fig. 9i and j), which coincides with the postglacial Meltwater Pulse 1a (MWP1a); a period marked by rapid global sea-level rise of 16–25 m within 400–500 years (Cronin, 2012, and references therein).

Reconstructions of the southern Red Sea palaeoshorelines, however, suggest that the sea-level rise during MWP1a did not sufficiently reduce the extent of the exposed shelf to independently and fully account for such an abrupt shift in the sedimentary regime. Importantly, until the onset of the Holocene at 11.7 ka (sea-level at 60 m below present) much of the southern shelf remained exposed and continued to serve as a potential source of detrital material (Fig. 10b). By the middle Holocene (ca. 7 ka), sea level had risen to approximately 10 m below the present level, likely submerging most of the continental shelf (Fig. 10c). While the exact timing of the complete shelf flooding remains uncertain, it is reasonable to infer that the exposed shelf continued to potentially serve as an additional detrital source to our site until ca. 7 ka.

Another sea-level rise-related mechanism that may have influenced sedimentation at our site is the dilution of the terrestrial component by an abrupt increase of biogenic material from ca. 15.4 ka onwards (Sergiou et al., 2022a). This mechanism has been previously proposed for the southern (Bouilloux et al., 2013b) and central (Ehrmann et al., 2024) Red Sea, and for other continental margin studies in the tropical and subtropical Atlantic (Govin et al., 2012), and Andaman Sea (Gebregiorgis et al., 2020). However, mass accumulation rates of the FA09 detrital (Fig. 11h), carbonate (Fig. 9h), and organic carbon (Fig. 9a) components indicate that the decline in terrestrial input and increase in biogenic input occurred largely independently during the rapid sea-level rise from ca. 15.4 to ca. 11 ka, with both processes contributing to the major transition observed across all proxies between ca. 15.4 and ca. 14.6 ka. While we cannot entirely rule out a potential dilution of the detrital signal due to sea-level rise-related productivity increases, the timing of this detrital decrease aligns with that observed in other Red Sea and western Arabian records during the last Deglaciation (e.g., Palchan and Torfstein, 2019; Pourmand et al., 2007), further indicating that dilution is unlikely to be the primary mechanism controlling sedimentary composition.

Following the MWP1a event, pronounced oceanographic modifications appear to occur in the southern Red Sea, driven by both the inflow of nutrient-rich water masses from the Gulf of Aden and enhanced local

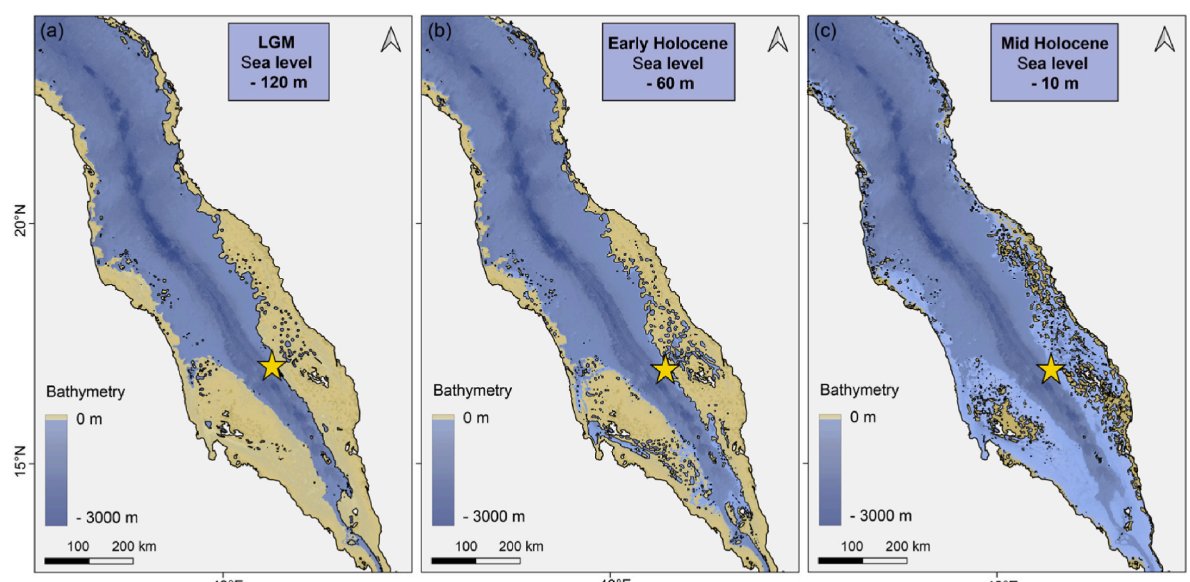

Fig. 10. Reconstructions of the southern Red Sea palaeoshorelines including (a) the LGM (ca. 20 ka) palaeoshoreline at 120 m below the present sea-level (b) the early Holocene (ca. 11.7 ka), palaeoshoreline at 60 m below the present sea-level, and (c) the middle Holocene (ca. 7 ka) palaeoshoreline at 10 m below the present sea-level. The yellow star marks the position of the FA09 core. Sandy-brown areas indicate the surface of the exposed continental shelf for the three phases. (b) At the onset of the Holocene a large part of the continental shelf remains exposed. High-resolution bathymetric data from the DISPERSE cruise (Sakellariou et al., 2019) were combined with the GEBCO Gridded Bathymetry (GEBCO 2024 Grid) in order to create the final bathymetric maps. For the Red Sea Relative Sea Level (RSL) reconstruction, data were combined from: i) Al-Mikhlafi et al. (2021); 7–0 kyr, ii) Arz et al. (2007); 23–13 kyr, and iii) Grant et al. (2012); 31–23 kyr and 13–7 kyr. (For interpretation of the references to colour in this figure legend, the reader is referred to the Web version of this article.)

upwelling processes (Sergiou et al., 2022a). Weak laminations (Fig. 4b) and a substantial increase in the Br content (Fig. 9c) suggest bottom-water anoxia and potentially increased surface productivity between ca. 15.4 ka and ca. 10 ka. This is further corroborated by the abrupt surge in TOC fluxes and concentrations (Fig. 9a and b) and the significantly increased dysoxic benthic foraminiferal assemblages (Fig. 9d) and planktic foraminifera taxa (Fig. 9e), which altogether point to an intensified oxygen minimum zone (OMZ) and high water-column stratification (Sergiou et al., 2022b).

Another noteworthy observation is the substantial increase of the aragonite content from ca. 14.6 ka onwards (Fig. 9f). In contrast to these findings, previous studies from the Red Sea have reported an enhanced or even complete aragonite dissolution during interglacial periods with well-ventilated bottom waters, and greater preservation during glacial periods with anoxic bottom-water conditions (e.g., Almogi-Labin et al., 1998, 1986). Moreover, inorganic aragonite precipitation has been documented during the highly saline and supersaturated conditions of glacial sea-level lowstands (Almogi-Labin et al., 1986; Fenton et al., 2000; Milliman et al., 1969; Rohling et al., 1998). The preservation of aragonite at the FA09 site is likely attributed to the site's position relative to the OMZ, which currently occurs at depths between 200 and 650 m (Edelman-Furstenberg et al., 2001; Weikert, 1982). The above-mentioned studies reporting interglacial aragonite dissolution are located within intermediate or deeper water masses, beneath the OMZ, where the well-oxygenated waters facilitate this process. Moreover, these sites are closer to or within the northern Red Sea section, where the formation of oxygen-rich deep water takes place, further enhancing this dissolution process (e.g., Almogi-Labin et al., 1998). Currently situated at a relatively shallow depth of 302 m, the FA09 site remains within the oxygen-depleted conditions of the OMZ, where oxygen concentrations range around 0.5 ml O_2/l, between 300 and 400 m, near the Bab al Mandab area (Fenton et al., 2000; Neumann and McGill, 1961). Given the similar, or potentially greater, extent of the OMZ following the deglacial sea-level rise (Almogi-Labin et al., 1991), it is plausible to assume that the FA09 core has been persistently located within this zone, enabling the preservation of aragonite in the sediment. A similar pattern of aragonite deposition under a well-stratified water column and low-oxygen seafloor conditions has also been documented during times of increased sea-level rise in the semi-enclosed Gulf of Corinth (Sergiou et al., 2024).

6.3. Atmospheric and hydroclimatic imprints on the southern Red Sea sedimentation

Superimposed on the long-term sea-level-related imprints on sedimentation, variations in terrestrial proxy records from Core FA09 can further reflect the shorter-term hydroclimatic variability that prevails in the surrounding region. The overall declining trend observed in all detrital proxies from ca. 30 to ca. 0.8 ka appears to correspond to both global and regional patterns, indicating higher dust fluxes during glacial periods and lower fluxes during interglacial periods (e.g., Lambert et al., 2008; Maher et al., 2010; Roberts et al., 2011).

While the detrital concentrations (Fig. 6a) exhibit two relatively stable and distinct phases throughout the record separated by an abrupt shift at ca. 14.6 ka, detrital fluxes (Fig. 11h) show a few pronounced peaks, superimposed on a generally decreasing trend between ca. 30 and 0.8 ka. More specifically, the relatively enhanced detrital signal is coarse-grained (centered around 52 μm) between ca. 30 and ca. 14.6 ka (Fig. 11f), and predominately composed of illite (Fig. S6h) and quartz (Fig. 11g). This composition suggests a strong granitic and metamorphic contribution, consistent with findings from Sr-Nd isotopic studies in the northern (Core KL23; Palchan et al., 2013), central (Core KL11; Palchan et al., 2013), and southern Red Sea (Core MD8; Rojas et al., 2019). The isotopic signatures of the proximal MD8 (southern Red Sea), and MD2 (Gulf of Aden) records suggest a probable granitic origin linked to the ANS, with additional contributions from the Saharan granitoids and quartz-rich rhyolitic material from the Ethiopian Highlands (Rojas et al., 2019). Higher smectite contents and greater radiogenic ε_{Nd} values of Cores MD8 and MD2, however, point to an additional basaltic input from the Afar region which appears to be more pronounced during the glacial period in both records (Rojas et al., 2019). In a similar manner, high smectite contents and the detrital Sr and Nd isotopic compositions in Core KL11 suggest a predominant basaltic dust input through the Tokar Gap (Ehrmann et al., 2024). In contrast, the mineralogical composition of FA09 indicates no evidence of such a basaltic component throughout the entire record, as key basaltic minerals such as plagioclase and pyroxene – both present in the bulk mineralogical MD8 and MD2 records – are absent.

This absence of a basaltic signal from the Afar region in the FA09 core could possibly be related to regional sediment transport vectors which govern dust transport and influence its deposition in our study area. Modern wind circulation patterns show that the FA09 site is situated within the trajectory of two major dust-bearing atmospheric systems which are especially pronounced during the summer months (Fig. 2c and d). Namely, the mid-latitude westerlies (e.g., Woor et al., 2022) which can carry large amounts of mostly granitic material from the ANS, and the eastward winds funneled through the Tokar Gap Jet (Davis et al., 2015; Jiang et al., 2009) that can transport weathering products of the Ethiopian Highland basalts (Ehrmann et al., 2024; Hickey and Goudie, 2007) (Fig. 2a–c). The northeast monsoon (NEM) wind that is channeled through the Bab al Mandab strait towards the southern Red Sea during the winter (Fig. 2b–d) seems to play a minor role in sediment transport towards the FA09 site, as previous studies suggest it only carries minimal dust loads from the Arabian Peninsula (Leuschner and Sirocko, 2000; Sirocko and Lange, 1991). The predominance of a granitic signal in the FA09 record potentially suggests a much stronger influence of material transported from the ANS via the mid-latitude westerlies to our study site. Rojas et al. (2019), however, suggest that the glacial basaltic signal in the southern Red Sea and the Gulf of Aden records is either transported by the northwesterlies or by low-altitude winds which are channelled through the Red Sea during the summer months. In any case, we must note that the lack of a basaltic signal in our mineralogical record can also be attributed to methodological constraints. While bulk proxies such as the mineralogical, geochemical and detrital grain-size compositions can theoretically provide insights into source areas (e.g., Grousset and Biscaye, 2005), isotopic elemental analysis remains essential to reliably distinguish the detrital sources represented in the FA09 record (e.g., Ehrmann et al., 2024; Palchan et al., 2018; Rojas et al., 2019; Stein et al., 2007).

Despite some discrepancies amongst records, pronounced coarse-grained detrital fluxes are consistently observed in the Red Sea, Gulf of Aden and western Arabian Sea and reflect the prevailing continental aridity and intensified physical weathering processes that persisted during the glacial (Clemens et al., 1991; Clemens and Prell, 1990; Palchan et al., 2013; Thunell et al., 1988). For example, Core KL11 from the central Red Sea exhibits a comparably-sized (65 μm) coarse detrital signal to FA09 that prevails until ca. 14 ka and is attributed to aeolian transport (Fig. 2b in Ehrmann et al. (2024)). Likewise, the coarse detrital glacial modes (centered around 50 μm) in other records from the southern Red Sea (MD8) and Gulf of Aden (MD2) persist until approximately 14–15 ka, and have been attributed to detrital input from rather proximal sediment sources (Fig. 4a in Rojas et al. (2019)). In a similar manner, dust fluxes from Core RC27-42 in the western Arabian Sea remain elevated up until ca. 17 ka (Pourmand et al., 2007) (Fig. 11e).

Interestingly, the 500 kyr Ti/Ca dust record from Core KL09 in the central Red Sea indicates that the highest dust fluxes occur during glacial terminations rather than glacial stages (Roberts et al., 2011). In contrast, the FA09 Ti/Ca record (Fig. 11b) remains relatively stable throughout the glacial period, though low-amplitude fluctuations are observed between ca. 17 ka and ca. 14.6 ka, closely resembling those in the GeoB5844-2 Ti/Ca record from the northern Red Sea (Arz et al., 2003) (Fig. 11a). During the same period, the FA09 detrital flux record

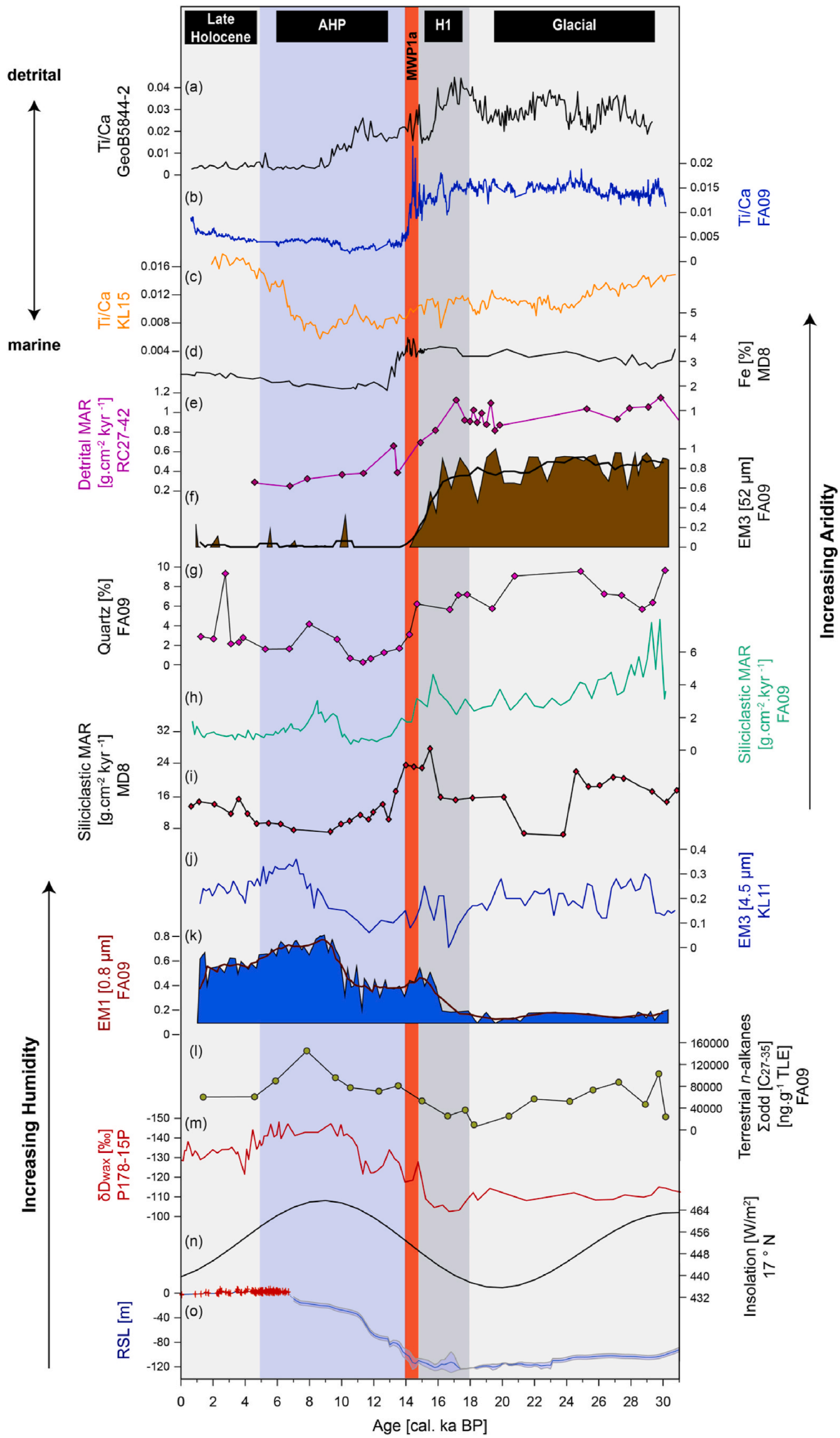

(caption on next page)

Fig. 11. Compilation of detrital records from the Red Sea and the Gulf of Aden. Shaded areas mark the timing of the Heinrich event 1 (H1), the Meltwater Pulse 1a (MWP1a), and the African Humid Period (AHP) as discussed in the text. (a) XRF-CS Ti/Ca ratio from Core GeoB5844-2, northern Red Sea (Arz et al., 2003), (b) the MLC-predicted Ti/Ca ratio from Core FA09 (this study), (c) the Ti/Ca ratio from Core KL15, Gulf of Aden (Fischer et al., 2024), (d) Fe content from Core MD8, southern Red Sea (Bouilloux et al., 2013b), (e) detrital fluxes from Core RC27-42, western Arabian Sea (Pourmand et al., 2007), (f) EM3 [52 μm] of the siliciclastic grain-size fraction from Core FA09 (this study), (g) quartz concentrations from Core FA09 (this study), (h) the siliciclastic mass accumulation rates (MARs) from Core FA09 (this study), (i) the siliciclastic mass accumulation rates (MARs) from Core MD8, southern Red Sea (Rojas et al., 2019), (j) EM3 [4.5 μm] of the siliciclastic grain-size fraction from Core KL11, central Red Sea (Ehrmann et al., 2024), (k) EM1 [0.8 μm] of the siliciclastic grain-size fraction from Core FA09 (this study), (l) sum of the terrestrial long-chain odd *n*-alkanes from Core FA09 (this study), (m) the δD_{wax} record from Core P178-15P, Gulf of Aden (Tierney and DeMenocal, 2013), (n) summer (June-July-August) insolation at 17 °N (Laskar et al., 2004), and (o) Red Sea Relative Sea Level (RSL) reconstruction, synthesized by combined data from Al-Mikhlafi et al. (2021) (red crosses), Arz et al. (2007), and Grant et al. (2012). (For interpretation of the references to colour in this figure legend, the reader is referred to the Web version of this article.)

exhibits a small but distinct peak (Fig. 11h), which, despite age-model uncertainties, closely aligns with a similar peak in the MD8 record (Rojas et al., 2019). This period coincides with both the Heinrich Event 1 (H1) (HE-sl1; 19–14.6 kyr), and with a phase of short-term sea-level fluctuations (Clark et al., 2004) that could have further impacted sediment transport to our study site. Across the Red Sea, Arabian Sea, and Gulf of Aden, these millennial-scale intense climatic Heinrich Events coincide with a southward displacement of the ITCZ, extreme widespread aridity driven by low monsoonal precipitation, intensified wind circulation and pronounced cooling (Arz et al., 2003; Deplazes et al., 2014; Roskin et al., 2011; Singh et al., 2016; Stager et al., 2011). While the imprint of H1 on the FA09 terrestrial signal appears weak, high sea-surface salinities, low sea-surface temperatures, $\delta^{18}O$ enrichment, and negligible planktic foraminifera fluxes in the same record indicate the influence of a strengthened, cool, and dry NEM wind system, which developed in response to the southward displacement of the ITCZ during H1 (Sergiou et al., 2022a).

As mentioned above, the most pronounced excursion in all of our proxy records occurs at ca. 15.4–14.6 kyr, marking the end of H1 and the onset of the Greenland Interstadial-1 (GI-1; 14.6–12.9 kyr). This noticeable shift is more or less evident throughout the entire Red Sea basin; as reflected in the Ti/Ca record from Core GeoB5844-2 in northern Red Sea (Arz et al., 2003) (Fig. 11a) and the Fe record from MD8 in the southern Red Sea (Rojas et al., 2019) (Fig. 11d). The GeoB5844-2 Ti/Ca record from the northern Red Sea shows a gradual decline between ca. 16 and ca. 9 ka, although it presents some notable short-term fluctuations during this period. Both the FA09 and MD8 records from the southern Red Sea exhibit an abrupt shift; however, the transition in MD8 occurs more gradually, between ca. 14.6 and ca. 13 ka, compared to the rapid change observed in FA09. Unlike the Red Sea records, the KL15 Ti/Ca record from the Gulf of Aden (Fig. 11c) follows an even more gradual trend, spanning from ca. 30 to ca. 8 ka, without any distinct abrupt shifts. This pronounced difference between the Gulf of Aden record and all the Red Sea records further highlights the dominant influence of sea-level and associated marine productivity increases throughout the Red Sea basin. While variations in wind circulation between the northern Red Sea, southern Red Sea, and Gulf of Aden can influence the timing and transport of detrital material, the pronounced difference between the Red Sea and Gulf of Aden records suggests a stronger influence of sea-level-driven marine productivity fluctuations on the Ti/Ca ratio.

Coinciding with this Ti/Ca shift, a major reduction in coarse-grained detrital material (Fig. 11f) and an increase in finer-grained material (Fig. 11k) suggest a shift in wind circulation and precipitation patterns in the region. The strong similarity between the fine detrital FA09 EM1 record (Fig. 11k) and the KL11 fluvial EM3 record from the central Red Sea (Fig. 11j) between ca. 16 and 0.8 ka further supports our interpretation of EM1 as fluvial in origin throughout this period. This similarity may also reflect comparable hydroclimatic conditions across these sections of the basin and, potentially, a common riverine influence from the Baraka Wadi on both sites. However, even if fluvial discharge from the Baraka Wadi did not directly influence our site, local wadi runoff from the Saudi Arabian coast (Fig. 1b) most likely contributed to sediment transport and deposition in our study area (Matter et al., 2016).

While we acknowledge the limitations of the low-resolution FA09 terrestrial *n*-alkane record, the increasing trend observed from ca. 16 ka onwards remains notable (Fig. 11l). Its resemblance to the fluvial EM1 record over the same period suggests a potential link between terrestrial higher-plant input and fluvial transport, while the increase in terrestrial *n*-alkanes from ca. 16 to ca. 8 ka may further indicate an expansion of vegetation biomass in the source areas, potentially driven by wetter conditions. This patter aligns with the 200 kyr-long terrestrial *n*-alkane flux record from the Gulf of Aden (GOA4), which suggests that pluvial conditions may have contributed to enhanced vegetation biomass in the region (Isaji et al., 2015).

Increased moisture availability during this time is consistent with the broader climatic changes associated with the AHP that affected East Africa and the Arabian Peninsula between ca. 15 and 5 ka. This period was marked by substantial increases in orbitally forced monsoon-driven summer precipitation (e.g. Foerster et al., 2012; Gasse, 2000; Tierney and DeMenocal, 2013). Although the atmospheric sources of this increased AHP precipitation have not been fully constrained, it is generally accepted that a northward and eastward advance of the ISM and ASM contributed to enhanced rainfall in the southern Arabian Peninsula and Red Sea region (Engel et al., 2017; Enzel et al., 2015; Guagnin et al., 2016; Jennings et al., 2015; Tierney and DeMenocal, 2013). Even though the FA09 *n*-alkane record (Fig. 11l) cannot discern vegetation type or directly infer hydroclimatic conditions, it closely corresponds with the δD_{wax} precipitation record from the Gulf of Aden, which suggests a rapid shift to wetter conditions in the Horn of Africa region during the AHP (Tierney and DeMenocal, 2013).

Following the wetter conditions of the AHP, a small increase in the Ti/Ca ratio (Fig. 11b), and the fine aeolian end-member (EM2) (Fig. 7b) indicate the re-establishment of arid conditions in the surrounding region from ca. 5 ka onwards. A concurrent decrease of the very fine, presumably fluvial end-member (EM1) (Fig. 11k) further supports a reduction in precipitation and, consequently, local wadi runoff, likely driven by declining northern hemisphere summer solar insolation (Fig. 11n) and the strengthening of the regional dry NEM wind system (e.g., Fleitmann et al., 2007; Gupta et al., 2003; Sergiou et al., 2022a; Van Rampelbergh et al., 2013). This transition towards less-humid conditions is also captured by an abrupt shift in the δD_{wax} records from the Gulf of Aden (Tierney et al., 2017; Tierney and DeMenocal, 2013) (Fig. 11m), and by a decrease in the fluvial end-member (EM3) from the central Red Sea (Ehrmann et al., 2024) (Fig. 11j). The enhanced siliciclastic fluxes of Core MD8 in the southern Red Sea (Rojas et al., 2019) (Fig. 11i), and the pronounced increase in the Ti/Ca ratio of Core KL15 in the Gulf of Aden (Fischer et al., 2024) (Fig. 11c) further corroborate this regional signal of enhanced late Holocene dust transport and aridity (Jung et al., 2004). Although the resolution of the FA09 *n*-alkane record is restrictive, it is noteworthy that terrestrial *n*-alkanes also show a modest decline during this period (Fig. 11l), further suggesting a weakening of transporting mechanisms such as fluvial discharge and/or a potential reduction of vegetation biomass. Future research is necessary to generate high-resolution isotopic datasets (δD and $\delta^{13}C$) to more robustly constrain the interplay between vegetation dynamics and regional sediment transport processes.

6.4. Archaeological implications

The previously discussed palaeoclimatic findings can also be placed within the broader context of the DISPERSE project, which was initiated to explore the potential archaeological significance of the now-submerged landscape as a zone of human occupation (Bailey, 2015; Bailey et al., 2015). The FA09 record was one of the many records recovered from the continental shelf in the vicinity of the Farasan Islands as part of this extensive project. The hypothesis that the continental shelf around the Farasan Islands could have served as a habitable zone and refugium for plants, animals and early humans during the sea-level lowstand of the LGM is based on the presence of numerous deep and potentially water-bearing sinkholes dotted across the exposed landscape, geomorphological evidence of shallow valleys shaped by fluvial erosion, and the likelihood of substantial groundwater availability from enhanced spring outflows under lower sea-level pressure (Faure et al., 2002; Sakellariou et al., 2019). While our results suggest prolonged aridity, sparse vegetation cover and no definitive evidence of surface run-off during the glacial, these data cannot constitute decisive evidence either for or against the hypothesis of human presence on the exposed continental shelf. This becomes even more apparent since the more favourable conditions associated with spring activity are likely to have been quite localised and, therefore, difficult to detect in an offshore location reflecting a regional catchment. In any case, human population densities on the exposed continental shelf were likely relatively low, with subsistence patterns requiring a high degree of mobility. Further insights into these issues may emerge from ongoing analysis of sediment cores recovered during the original survey from bathymetric depressions within the previously exposed subaerial landscape.

7. Conclusions

The (sub-)centennial-scale resolution sedimentological and geochemical proxy records from Core FA09 disclose the combined controls of sea-level and continental hydroclimate on the sedimentary dynamics of the southern Red Sea over the past 30 kyr. An increased accumulation of coarse-grained siliciclastic material, primarily of granitic origin, until ca. 14.6 ka reflects the prevalence of arid conditions and heightened wind circulation around the Red Sea during the glacial period. Between ca. 17 and 15 ka, a pronounced peak in detrital fluxes highlights the impact of H1 on the region, and is followed by a marked shift in most detrital proxies that aligns with the termination of H1 and the onset of GI-1, at ca. 14.6 ka. The imprint of deglacial sea-level rise is evident through the increase of marine biogenic carbonates, such as aragonite and calcite, suggesting the restoration of water-mass exchange with the Gulf of Aden and the influx of less saline and highly productive water masses from ca. 15 ka onwards. An influx of fine-grained fluvial material and terrestrial plant-wax biomarkers mark the onset of the AHP at ca. 15 ka and the associated establishment of more pluvial conditions in response to the expansion of African and Indian summer monsoon precipitation. Following the AHP, the re-establishment of arid conditions from ca. 5 ka onwards is indicated by a decrease of the fluvial detrital fraction and a small, yet steady, increase of the Ti/Ca ratio and of detrital minerals such as quartz.

CRediT authorship contribution statement

Francesca Paraschos: Conceptualization, Investigation, Data curation, Formal analysis, Funding acquisition, Writing - original draft, Writing - review & editing. **Andreas Koutsodendris:** Writing - original draft, Writing - review & editing. **Spyros Sergiou:** Investigation, Writing - review & editing. **Maria Geraga:** Writing - review & editing. **Helen Kaberi:** Investigation, Writing - review & editing. **Melissa Berke:** Investigation, Writing - review & editing. **Oliver Friedrich:** Writing - review & editing. **Stylianos Iliakis:** Investigation. **Mirko Alessandro Uy:** Investigation. **Ross Williams:** Investigation. **Geoffrey Bailey:** Conceptualization, Funding acquisition, Project administration, Writing - original draft, Writing - review & editing. **Dimitris Sakellariou:** Conceptualization, Funding acquisition, Project administration, Writing - original draft, Writing - review & editing.

Data availability statement

The datasets presented in this study will be made available upon publication and can be accessed via the following link: https://www.seanoe.org/data/00926/103813/

Funding

This research was funded by the European Research Council through ERC Advanced Grant 269586 "DISPERSE: Dynamic Landscapes, Coastal Environments and Human Dispersals" under the 'Ideas' Specific Programme of the Seventh Framework Programme. Francesca Paraschos acknowledges scholarship funding from the Hellenic Center for Marine Research (HCMR) during the full course of this research work, the European Association of Organic Geochemistry (EAOG) Research Grant (2019), the International Association of Sedimentologists (IAS) Postgraduate Research Grant (2021), the ERASMUS + Mobility program, and the International Union for Quaternary Research (INQUA) Fellowship Program for International Mobility (2023).

Declaration of competing interest

We declare that this manuscript has been approved for submission by all authors; that it is being submitted solely for consideration by *Quaternary Science Reviews,* and, that all data presented are unpublished. We have no conflicts of interest to disclose.

Acknowledgments

We would like to kindly acknowledge the captain and crew of the R/V AEGAEO during the 2013 DISPERSE Farasan research cruise. We would also like to thank the Saudi Commission for Tourism and National Heritage (SCTH) and the Department of General Survey of the Ministry of Defense for fieldwork permissions. We thank George Krokos, Karl J.F. Meier, Daniela J.M. Müller, and Jörg Pross for scientific discussions. Pavlos Avramidis, Afroditi Androni, Ariadne Argyraki, Michael Burchard, Vivi Drakopoulou, Giannis Fiskilis, Jaime Frigola, Ilse Glass, Katharina Hess, Kayla Hollister, Oliver A. Kern, Laurin S. Kolb, Zacharenia Kypritidou, Alkiviades Papageorgiou and Sönke Szidat are greatly thanked for their technical support. We sincerely thank Dominik Fleitmann (editor) and two anonymous reviewers for their insightful and constructive comments on our manuscript. This is DISPERSE contribution no. 67.

Appendix A. Supplementary data

Supplementary data to this article can be found online at https://doi.org/10.1016/j.quascirev.2025.109310.

Data availability

A link to the data and/or code is provided as part of this submission.

References

Abou-Ouf, M., Elshater, A., 1992. Sedimentology and mineralogy of Jizan shelf sediments Red Sea. Saudi Arabia. J. King Abdulaziz Univ. Sci. 3 (4), 39–54. https://doi.org/10.4197/mar.3-1.

Al-Mikhlafi, A.S., Hibbert, F.D., Edwards, L.R., Cheng, H., 2021. Holocene relative sea-level changes and coastal evolution along the coastlines of Kamaran Island and As-Salif Peninsula, Yemen, southern Red Sea. Quat. Sci. Rev. 252. https://doi.org/10.1016/j.quascirev.2020.106719.

Almalki, K.A., Bantan, R.A., 2016. Lithologic units and stratigraphy of the farasan Islands, southern Red Sea. Carbonates Evaporites 31, 115–128. https://doi.org/10.1007/s13146-015-0247-4.

Almogi-Labin, A., Hemleben, C., Meischner, D., 1998. Carbonate preservation and climatic changes in the central Red Sea during the last 380 kyr as recorded by pteropods. Mar. Micropaleontol. 33, 87–107. https://doi.org/10.1016/S0377-8398(97)00034-0.

Almogi-Labin, A., Luz, B., Duplessy, J.C., 1986. Quaternary paleo-oceanography, pteropod preservation and stable-isotope record of the Red Sea. Palaeogeogr. Palaeoclimatol. Palaeoecol. 57, 195–211. https://doi.org/10.1016/0031-0182(86)90013-1.

Almogi-Labin, A., Hemleben, C., Meischner, D., Erlenkeuser, H., 1991. Paleoenvironmental events during the last 13,000 years in the central Red Sea as recorded by pteropoda. Paleoceanography 6, 83–98. https://doi.org/10.1029/90PA01881.

Arz, H.W., Lamy, F., Ganopolski, A., Nowaczyk, N., Pätzold, J., 2007. Dominant Northern Hemisphere climate control over millennial-scale glacial sea-level variability. Quat. Sci. Rev. 26, 312–321. https://doi.org/10.1016/j.quascirev.2006.07.016.

Arz, H.W., Pätzold, J., Müller, P.J., Moammar, M.O., 2003. Influence of Northern Hemisphere climate and global sea level rise on the restricted Red Sea marine environment during termination I. Paleoceanography 18, 1053. https://doi.org/10.1029/2002pa000864.

Bailey, G., 2015. The evolution of the Red Sea as a human habitat during the quaternary period 599–614. https://doi.org/10.1007/978-3-662-45201-1_34.

Bailey, G.N., Devès, M.H., Inglis, R.H., Meredith-Williams, M.G., Momber, G., Sakellariou, D., Sinclair, A.G.M., Rousakis, G., Al Ghamdi, S., Alsharekh, A.M., 2015. Blue Arabia: Palaeolithic and underwater survey in SW Saudi Arabia and the role of coasts in Pleistocene dispersals. Quat. Int. 382, 42–57. https://doi.org/10.1016/j.quaint.2015.01.002.

Bailey, G.N., Meredith-Williams, M., Alsharekh, A.M., Hausmann, N., 2019. The archaeology of pleistocene coastal environments and human dispersal in the Red Sea: insights from the farasan Islands. In: Rasul, N.M.A., Stewart, I.C.F. (Eds.), Geological Setting, Palaeoenvironment and Archaeology of the Red Sea. Springer Berlin Heidelberg, pp. 587–608. https://doi.org/10.1007/978-3-319-99408-6_26.

Basaham, A.S., 2009. Geochemistry of jizan shelf sediments, southern Red Sea coast of Saudi Arabiaجيوكيميائية رواسب رصيف جيزان ، الساحل الجنوبي للبحر الأحمر - المملكة العربية السعودية. Arab. J. Geosci. 2, 301–310. https://doi.org/10.1007/s12517-009-0033-5.

Belkin, I.M., 2009. Rapid warming of large marine ecosystems. Prog. Oceanogr. 81, 207–213. https://doi.org/10.1016/j.pocean.2009.04.011.

Bentor, Y.K., 1985. The crustal evolution of the Arabo-Nubian Massif with special reference to the Sinai Peninsula. Precambr. Res. 28, 1–74. https://doi.org/10.1016/0301-9268(85)90074-9.

Berke, M.A., Johnson, T.C., Werne, J.P., Schouten, S., Sinninghe Damsté, J.S., 2012. A mid-Holocene thermal maximum at the end of the African Humid Period. Earth Planet Sci. Lett. 351–352, 95–104. https://doi.org/10.1016/j.epsl.2012.07.008.

Bertrand, S., Tjallingii, R., Kylander, M.E., Wilhelm, B., Roberts, S.J., Arnaud, F., Brown, E., Bindler, R., 2024. Inorganic geochemistry of lake sediments: a review of analytical techniques and guidelines for data interpretation. Earth-Science Rev. 249, 104639. https://doi.org/10.1016/j.earscirev.2023.104639.

Bindoff, N.L., Willebrand, J., Artale, V., Cazenave, A., Gregory, J., Gulev, S., Hanawa, K., Le Quéré, C., Levitus, S., Nojiri, Y., Shum, C.K., Talley, L.D., Unnikrishnan, A., 2007. Observations: Oceanic climate change and Sea Level coordinating. Clim. Chang. 2007 Phys. Sci. Basis. Contrib. Work. Gr. I to Fourth Assess. Rep. Intergov. Panel Clim. Chang. 387–429.

Biton, E., Gildor, H., Peltier, W.R., 2008. Red Sea during the last glacial maximum: implications for sea level reconstruction. Paleoceanography 23, 1214. https://doi.org/10.1029/2007PA001431.

Blaauw, M., Christen, J.A., 2011. Flexible paleoclimate age-depth models using an autoregressive gamma process. Bayesian Anal 6, 457–474. https://doi.org/10.1214/11-ba618.

Blanchet, C.L., Ramisch, A., Tjallingii, R., Ionita, M., Laruelle, L., Bagge, M., Klemann, V., Brauer, A., 2024. Climatic pacing of extreme nile floods during the North African Humid Period. Nat. Geosci. https://doi.org/10.1038/s41561-024-01471-9.

Böning, P., Bard, E., 2009. Millennial/centennial-scale thermocline ventilation changes in the Indian Ocean as reflected by aragonite preservation and geochemical variations in Arabian Sea sediments. Geochim. Cosmochim. Acta 73, 6771–6788. https://doi.org/10.1016/j.gca.2009.08.028.

Bouilloux, A., Valet, J.P., Bassinot, F., Joron, J.L., Blanc-Valleron, M.M., Moreno, E., Dewilde, F., Kars, M., Lagroix, F., 2013a. Diagenetic modulation of the magnetic properties in sediments from the Northern Indian Ocean. Geochemistry, Geophys. Geosystems 14, 3779–3800. https://doi.org/10.1002/ggge.20234.

Bouilloux, A., Valet, J.P., Bassinot, F., Joron, J.L., Dewilde, F., Blanc-Valleron, M.M., Moreno, E., 2013b. Influence of seawater exchanges across the bab-el-mandeb strait on sedimentation in the southern Red Sea during the last 60 ka. Paleoceanography 28, 675–687. https://doi.org/10.1002/2013PA002544.

Caliñski, T., Harabasz, J., 1974. A dendrite method foe cluster analysis. Commun. Stat 3, 1–27. https://doi.org/10.1080/03610927408827101.

Cerdà-Domènech, M., Frigola, J., Sanchez-Vidal, A., Canals, M., 2020. Calibrating high resolution XRF core scanner data to obtain absolute metal concentrations in highly polluted marine deposits after two case studies off Portmán Bay and Barcelona, Spain. Sci. Total Environ. 717, 134778. https://doi.org/10.1016/j.scitotenv.2019.134778.

Clark, P.U., McCabe, A.M., Mix, A.C., Weaver, A.J., 2004. Rapid rise of sea level 19,000 years ago and its global implications. Science 304, 1141–1144. https://doi.org/10.1126/science.1094449.

Clemens, S., Prell, W., Murray, D., Shimmield, G., Weedon, G., 1991. Forcing mechanisms of the Indian Ocean monsoon. Nature 353, 720–725. https://doi.org/10.1038/353720a0.

Clemens, S.C., Prell, W.L., 1990. Late Pleistocene variability of Arabian Sea summer monsoon winds and continental aridity: Eolian records from the lithogenic component of deep-sea sediments. Paleoceanography 5, 109–145. https://doi.org/10.1029/PA005i002p00109.

Crocker, A.J., Naafs, B.D.A., Westerhold, T., James, R.H., Cooper, M.J., Röhl, U., Pancost, R.D., Xuan, C., Osborne, C.P., Beerling, D.J., Wilson, P.A., 2022. Astronomically controlled aridity in the Sahara since at least 11 million years ago. Nat. Geosci. 15, 671–676. https://doi.org/10.1038/s41561-022-00990-7.

Cronin, T.M., 2012. Rapid sea-level rise. Quat. Sci. Rev. 56, 11–30. https://doi.org/10.1016/j.quascirev.2012.08.021.

Croudace, I.W., Rothwell, R.G., 2015. Micro-XRF studies of sediment cores. Applications of a Non-destructive Tool for the Environmental Sciences. Springer. https://doi.org/10.1515/logos-2016-0008.

Deplazes, G., Lückge, A., Stuut, J.-B.W.B.W., Pätzold, J., Kuhlmann, H., Husson, D., Fant, M., Haug, G.H., 2014. Weakening and strengthening of the Indian monsoon during Heinrich events and Dansgaard-Oeschger oscillations. Paleoceanography 29, 99–114. https://doi.org/10.1002/2013PA002509.

Develle, A.L., Gasse, F., Vidal, L., Williamson, D., Demory, F., Van Campo, E., Ghaleb, B., Thouveny, N., 2011. A 250ka sedimentary record from a small karstic lake in the Northern Levant (Yammoûneh, Lebanon). Paleoclimatic implications. Palaeogeogr. Palaeoclimatol. Palaeoecol. 305, 10–27. https://doi.org/10.1016/j.palaeo.2011.02.008.

Diegor, W., Longerich, H., Abrajano, T., Horn, I., 2001. Applicability of a high pressure digestion technique to the analysis of sediment and soil samples by inductively coupled plasma-mass spectrometry. Anal. Chim. Acta 431, 195–207. https://doi.org/10.1016/S0003-2670(00)01339-8.

Dietze, E., Hartmann, K., Diekmann, B., Ijmker, J., Lehmkuhl, F., Opitz, S., Stauch, G., Wünnemann, B., Borchers, A., 2012. An end-member algorithm for deciphering modern detrital processes from lake sediments of Lake Donggi Cona, NE Tibetan Plateau, China. Sediment. Geol. 243–244, 169–180. https://doi.org/10.1016/j.sedgeo.2011.09.014.

Dietze, M., Dietze, E., 2019. Package "EMMAgeo" Title End-Member Modelling of Grain-Size Data.

Doney, S.C., Fabry, V.J., Feely, R.A., Kleypas, J.A., 2009. Ocean acidification: the other CO2 problem. Ann. Rev. Mar. Sci 1, 169–192. https://doi.org/10.1146/annurev.marine.010908.163834.

Doney, S.C., Ruckelshaus, M., Emmett Duffy, J., Barry, J.P., Chan, F., English, C.A., Galindo, H.M., Grebmeier, J.M., Hollowed, A.B., Knowlton, N., Polovina, J., Rabalais, N.N., Sydeman, W.J., Talley, L.D., 2012. Climate change impacts on marine ecosystems. Ann. Rev. Mar. Sci 4, 11–37. https://doi.org/10.1146/annurev-marine-041911-111611.

Douville, H., Qasmi, S., Ribes, A., Bock, O., 2022. Global warming at near-constant tropospheric relative humidity is supported by observations. Commun. Earth Environ. https://doi.org/10.1038/s43247-022-00561-z.

Dullo, W.C., Montaggioni, L., 1998. Modern Red Sea coral reefs: a review of their morphologies and zonation. In: Sedimentation and Tectonics in Rift Basins Red Sea:-Gulf of Aden, pp. 583–594.

Edelman-Furstenberg, Y., Scherbacher, M., Hemleben, C., Almogi-Labin, A., 2001. Deep-sea benthic foraminifera from the central Red Sea. J. Foraminifer. Res. 31, 48–59. https://doi.org/10.2113/0310048.

Eglinton, G., Hamilton, R.J., 1967. Leaf epicuticular waxes. Science 156, 1322–1335.

Ehrmann, W., Wilson, P.A., Arz, H.W., Schulz, H., Schmiedl, G., 2024. Monsoon-driven changes in aeolian and fluvial sediment input to the central Red Sea recorded throughout the last 200000 years. Clim. Past 20, 37–52. https://doi.org/10.5194/cp-20-37-2024.

Engel, M., Matter, A., Parker, A.G., Parton, A., Petraglia, M.D., Preston, G.W., Preusser, F., Enzel, Y., Quade, J., Kushnir, Y., 2017. Lakes or wetlands? A comment on 'The middle Holocene climatic records from Arabia: Reassessing lacustrine environments, shift of ITCZ in Arabian Sea, and impacts of the southwest Indian and African monsoons' by Enzel et al. Glob. Planet. Change 148, 258–267. https://doi.org/10.1016/j.gloplacha.2016.11.001.

Enzel, Y., Kushnir, Y., Quade, J., 2015. The middle Holocene climatic records from Arabia: Reassessing lacustrine environments, shift of ITCZ in Arabian Sea, and impacts of the southwest Indian and African monsoons. Glob. Planet. Change 129, 69–91. https://doi.org/10.1016/j.gloplacha.2015.03.004.

Faure, H., Walter, R.C., Grant, D.R., 2002. The coastal oasis: ice age springs on emerged continental shelves. Glob. Planet. Change 33, 47–56. https://doi.org/10.1016/S0921-8181(02)00060-7.

Fenton, M., Geiselhart, S., Rohling, E.J., Hemleben, C., 2000. Aplanktonic zones in the Red Sea. Mar. Micropaleontol. 277–294. https://doi.org/10.1016/S0377-8398(00)00042-6.

Finch, A.A., Allison, N., 2007. Coordination of Sr and Mg in calcite and aragonite. Mineral. Mag. 71, 539–552. https://doi.org/10.1180/minmag.2007.071.5.539.

Fischer, M.L., Munz, P.M., Asrat, A., Foerster, V., Kaboth-Bahr, S., Marwan, N., Schaebitz, F., Schwanghart, W., Trauth, M.H., 2024. Spatio-temporal variations of climate along possible African-Arabian routes of H. sapiens expansion. Quat. Sci. Adv. 14, 100174. https://doi.org/10.1016/j.qsa.2024.100174.

Fleitmann, D., Burns, S.J., Mangini, A., Mudelsee, M., Kramers, J., Villa, I., Neff, U., Al-Subbary, A.A., Buettner, A., Hippler, D., Matter, A., 2007. Holocene ITCZ and Indian monsoon dynamics recorded in stalagmites from Oman and Yemen (Socotra). Quat. Sci. Rev. 26, 170–188. https://doi.org/10.1016/j.quascirev.2006.04.012.

Fleitmann, D., Burns, S.J., Mudelsee, M., Neff, U., Kramers, J., Mangini, A., Matter, A., 2003. Holocene forcing of the Indian monsoon recorded in a stalagmite from

Southern Oman. Science 300, 1737–1739. https://doi.org/10.1126/science.1083130.
Fleitmann, D., Burns, S.J., Pekala, M., Mangini, A., Al-Subbary, A., Al-Aowah, M., Kramers, J., Matter, A., 2011. Holocene and Pleistocene pluvial periods in Yemen, southern Arabia. Quat. Sci. Rev. 30, 783–787. https://doi.org/10.1016/j.quascirev.2011.01.004.
Foerster, V., Junginger, A., Langkamp, O., Gebru, T., Asrat, A., Umer, M., Lamb, H.F., Wennrich, V., Rethemeyer, J., Nowaczyk, N., Trauth, M.H., Schaebitz, F., 2012. Climatic change recorded in the sediments of the Chew Bahir basin, southern Ethiopia, during the last 45,000 years. Quat. Int. 274, 25–37. https://doi.org/10.1016/j.quaint.2012.06.028.
Folk, R.L., Ward, W.C., 1957. Brazos River Bar: A Study in the Significance of Grain Size Parameters.
Gasse, F., 2000. Hydrological changes in the African tropics since the last glacial maximum. Quat. Sci. Rev. 19, 189–211. https://doi.org/10.1016/S0277-3791(99)00061-X.
Gebregiorgis, D., Giosan, L., Hathorne, E.C., Anand, P., Nilsson-Kerr, K., Plass, A., Lückge, A., Clemens, S.C., Frank, M., 2020. What can we learn from X-ray fluorescence core scanning data? A paleomonsoon case study. Geochemistry, Geophys. Geosystems 21. https://doi.org/10.1029/2019GC008414.
Govin, A., Holzwarth, U., Heslop, D., Ford Keeling, L., Zabel, M., Mulitza, S., Collins, J. A., Chiessi, C.M., 2012. Distribution of major elements in Atlantic surface sediments (36°N-49°S): imprint of terrigenous input and continental weathering. Geochemistry, Geophys. Geosystems 13, 1–23. https://doi.org/10.1029/2011GC003785.
Grant, K.M., Rohling, E.J., Ramsey, C.B., Cheng, H., Edwards, R.L., Florindo, F., Heslop, D., Marra, F., Roberts, A.P., Tamisiea, M.E., Williams, F., 2014. Sea-level variability over five glacial cycles. Nat. Commun. 5, 1–9. https://doi.org/10.1038/ncomms6076.
Grant, K.M., Rohling, E.J., Bar-Matthews, M., Ayalon, A., Medina-Elizalde, M., Ramsey, C.B., Satow, C., Roberts, A.P., 2012. Rapid coupling between ice volume and polar temperature over the past 150,000 years. Nature 491, 744–747. https://doi.org/10.1038/nature11593.
Groucutt, H.S., Petraglia, M.D., Bailey, G., Scerri, E.M.L., Parton, A., Clark-Balzan, L., Jennings, R.P., Lewis, L., Blinkhorn, J., Drake, N.A., Breeze, P.S., Inglis, R.H., Dev Es, M.H., Meredith-Williams, M., Boivin, N., Thomas, M.G., Scally, A., 2015. Rethinking the dispersal of Homo sapiens out of africa. Evol. Anthropol. 24, 149–164. https://doi.org/10.1002/evan.21455.
Grousset, F.E., Biscaye, P.E., 2005. Tracing dust sources and transport patterns using Sr, Nd and Pb isotopes. Chem. Geol. 222, 149–167. https://doi.org/10.1016/j.chemgeo.2005.05.006.
Guagnin, M., Jennings, R., Eager, H., Parton, A., Stimpson, C., Stepanek, C., Pfeiffer, M., Groucutt, H.S., Drake, N.A., Alsharekh, A., Petraglia, M.D., 2016. Rock art imagery as a proxy for Holocene environmental change: a view from Shuwaymis, NW Saudi Arabia. Holocene 26, 1822–1834. https://doi.org/10.1177/0959683616645949.
Gupta, A.K., Anderson, D.M., Overpeck, J.T., 2003. Abrupt changes in the asian Southwest Monsoon during the Holocene and their links to the North atlantic ocean. Nature 421, 354–357.
Hartman, A., Torfstein, A., Almogi-Labin, A., 2020. Climate swings in the northern Red Sea over the last 150,000 years from εNd and Mg/Ca of marine sediments. Quat. Sci. Rev. 231, 106205. https://doi.org/10.1016/j.quascirev.2020.106205.
Heaton, T.J., Köhler, P., Butzin, M., Bard, E., Reimer, R.W., Austin, W.E.N., Bronk Ramsey, C., Grootes, P.M., Hughen, K.A., Kromer, B., Reimer, P.J., Adkins, J., Burke, A., Cook, M.S., Olsen, J., Skinner, L.C., 2020. Marine20-the marine radiocarbon age calibration curve (0-55,000 cal BP) Enhanced Reader.pdf. Radiocarbon 62, 779–820. https://doi.org/10.1017/RDC.2020.68.
Held, I.M., Soden, B.J., 2006. Robust responses of the hydrological cycle to global warming. J. Clim. 19, 5686–5699.
Hersbach, H., Bell, B., Berrisford, P., Biavati, G., Horányi, A., Muñoz Sabater, J., Nicolas, J., Peubey, C., Radu, R., Rozum, I., Schepers, D., Simmons, A., Soci, C., Dee, D., Thépaut, J.-N., 2023. ERA5 monthly averaged data on pressure levels from 1940 to present. Copernicus Clim. Chang. Serv. Clim. Data Store. https://doi.org/10.24381/cds.6860a573 (Accessed on DD-MMM-YYYY) [WWW Document].
Hickey, B., Goudie, A.S., 2007. The use of TOMS and MODIS to identify dust storm source areas: In: Goudie, A.S., Kalvoda, J. (Eds.), The Tokar Delta (Sudan) and the Seistan Basin (South West Asia), P3K, Prague. Geomorphological Variations, Prague, pp. 37–57.
Hodell, D., Crowhurst, S., Skinner, L., Tzedakis, P.C., Margari, V., Channell, J.E.T., Kamenov, G., MacLachlan, S., Rothwell, G., 2013. Response of Iberian Margin sediments to orbital and suborbital forcing over the past 420 ka. Paleoceanography 28, 185–199. https://doi.org/10.1002/palo.20017.
Hodell, D., Lourens, L., Crowhurst, S., Konijnendijk, T., Tjallingii, R., Jiménez-Espejo, F., Skinner, L., Tzedakis, P.C., Abrantes, F., Acton, G.D., Zarikian, C.A.A., Bahr, A., Balestra, B., Barranco, E.L., Carrara, G., Ducassou, E., Flood, R.D., José-Abel, Flores, Furota, S., Grimalt, J., Grunert, P., Hernández-Molina, J., Kim, J.K., Krissek, L.A., Kuroda, J., Li, B., Lofi, J., Margari, V., Martrat, B., Miller, M.D., Nanayama, F., Nishida, N., Richter, C., Rodrigues, T., Rodríguez-Tovar, F.J., Roque, A.C.F., Goñi, M. F.S., Sierro, F.J., Singh, A.D., Sloss, C.R., Stow, D.A.V., Takashimizu, Y., Tzanova, A., Voelker, A., Xuan, C., Williams, T., 2015. A reference time scale for site U1385 (Shackleton site) on the SW Iberian margin. Glob. Planet. Change 133, 49–64. https://doi.org/10.1016/j.gloplacha.2015.07.002.
Isaji, Y., Kawahata, H., Ohkouchi, N., Murayama, M., Tamaki, K., 2015. Terrestrial environmental changes around the Gulf of Aden over the last 210 kyr deduced from the sediment n-alkane record: implications for the dispersal of Homo sapiens. Geophys. Res. Lett. 42, 1880–1887. https://doi.org/10.1002/2015GL063196.
Jennings, R.P., Singarayer, J., Stone, E.J., Krebs-Kanzow, U., Khon, V., Nisancioglu, K.H., Pfeiffer, M., Zhang, X., Parker, A., Parton, A., Groucutt, H.S., White, T.S., Drake, N. A., Petraglia, M.D., 2015. The greening of Arabia: multiple opportunities for human occupation of the Arabian Peninsula during the Late Pleistocene inferred from an ensemble of climate model simulations. Quat. Int. 382, 181–199. https://doi.org/10.1016/j.quaint.2015.01.006.
Jung, S.J.A., Davies, G.R., Ganssen, G.M., Kroon, D., 2004. Stepwise Holocene aridification in NE Africa deduced from dust-borne radiogenic isotope records. Earth Planet Sci. Lett. 221, 27–37. https://doi.org/10.1016/S0012-821X(04)00095-0.
Karger, D.N., Conrad, O., Böhner, J., Kawohl, T., Kreft, H., Soria-Auza, R.W., Zimmermann, N.E., Linder, H.P., Kessler, M., 2021. Climatologies at high resolution for the earth's land surface areas. EnviDat. https://doi.org/10.16904/envidat.22.
Karger, D.N., Conrad, O., Böhner, J., Kawohl, T., Kreft, H., Soria-Auza, R.W., Zimmermann, N.E., Linder, H.P., Kessler, M., 2017. Climatologies at high resolution for the earth's land surface areas. Sci. Data 4, 170122. https://doi.org/10.1038/sdata.2017.122.
Koutsodendris, A., Nakajima, K., Kaboth-Bahr, S., Berke, M.A., Franzese, A.M., Hall, I.R., Hemming, S.R., Just, J., Levay, L.J., Pross, J., Robinson, R., Barker, S., Brentegani, L., Caley, T., Cartagena-Sierra, A., Charles, C.D., Coenen, J.J., Crespin, J.G., Gruetzner, J., Han, X., Hines, S.K.V., Espejo, F.J.J., Kubota, K., Lathika, N., Norris, R. D., Dos Santos, T.P., Rolinson, J.M., Simon, M.H., Tangunan, D., van der Lubbe, J.J. L., Yamane, M., Zhang, H., 2021. A plio-pleistocene (C. 0–4 ma) cyclostratigraphy for iodp site u1478 (Mozambique channel, sw indian ocean): Exploring an offshore record of paleoclimate and ecosystem variability in se africa. Newsletters Stratigr 54, 159–181. https://doi.org/10.1127/nos/2020/0608.
Lambeck, K., Purcell, A., Flemming, N.C., Vita-Finzi, C., Alsharekh, A.M., Bailey, G.N., 2011. Sea level and shoreline reconstructions for the Red Sea: Isostatic and tectonic considerations and implications for hominin migration out of Africa. Quat. Sci. Rev. 30, 3542–3574. https://doi.org/10.1016/j.quascirev.2011.08.008.
Lambert, F., Delmonte, B., Petit, J.R., Bigler, M., Kaufmann, P.R., Hutterli, M.A., Stocker, T.F., Ruth, U., Steffensen, J.P., Maggi, V., 2008. Dust - climate couplings over the past 800,000 years from the EPICA Dome C ice core. Nature 452, 616–619. https://doi.org/10.1038/nature06763.
Langodan, S., Cavaleri, L., Pomaro, A., Portilla, J., Abualnaja, Y., Hoteit, I., 2018. Unraveling climatic wind and wave trends in the Red Sea using wave spectra partitioning. J. Clim. 31, 1881–1895. https://doi.org/10.1175/JCLI-D-17-0295.1.
Larrasoaña, J.C., Roberts, A.P., Rohling, E.J., 2013. Dynamics of green Sahara periods and their role in hominin evolution. PLoS One 8. https://doi.org/10.1371/journal.pone.0076514.
Larrasoaña, J.C., Roberts, A.P., Rohling, E.J., Winklhofer, M., Wehausen, R., 2003. Three million years of monsoon variability over the northern Sahara. Clim. Dyn. 21, 689–698. https://doi.org/10.1007/s00382-003-0355-z.
Laskar, J., Robutel, P., Joutel, F., Gastineau, M., Correia, A.C.M., Levrard, B., 2004. A long-term numerical solution for the insolation quantities of the Earth. Astron. Astrophys. 428, 261–285. https://doi.org/10.1051/0004-6361:20041335.
Lehner, B., Grill, G., 2013. Global river hydrography and network routing: Baseline data and new approaches to study the world's large river systems. Hydrol. Process. 27, 2171–2186. https://doi.org/10.1002/hyp.9740.
Lézine, A.M., Bassinot, F., Peterschmitt, J.Y., 2014. Orbitally-induced changes of the Atlantic and Indian monsoons over the past 20,000years: new insights based on the comparison of continental and marine records. Bull. la Soc. Geol. Fr 185, 3–12. https://doi.org/10.2113/gssgfbull.185.1.3.
Maher, B.A., Prospero, J.M., Mackie, D., Gaiero, D., Hesse, P.P., Balkanski, Y., 2010. Global connections between aeolian dust, climate and ocean biogeochemistry at the present day and at the last glacial maximum. Earth-Science Rev. 99, 61–97. https://doi.org/10.1016/j.earscirev.2009.12.001.
Marzi, R., Torkelson, B.E., Olson, R.K., 1993. A revised carbon preference index. Org. Geochem. 20, 1303–1306. https://doi.org/10.1016/0146-6380(93)90016-5.
Matter, A., Mahjoub, A., Neubert, E., Preusser, F., Schwalb, A., Szidat, S., Wulf, G., 2016. Reactivation of the Pleistocene trans-Arabian Wadi ad Dawasir fluvial system (Saudi Arabia) during the Holocene humid phase. Geomorphology 270, 88–101. https://doi.org/10.1016/j.geomorph.2016.07.013.
McGee, D., Broecker, W.S., Winckler, G., 2010. Gustiness: the driver of glacial dustiness? Quat. Sci. Rev. 29, 2340–2350. https://doi.org/10.1016/j.quascirev.2010.06.009.
Meyers, P.A., 1994. Preservation of elemental and isotopic source identification of sedimentary organic matter. Chem. Geol. 114, 289–302.
Milliman, J.D., 1974. Marine Carbonates. Springer-Verlag.
Milliman, J.D., Ross, D.A., Ku, T.-L., 1969. Precipitation and lithification of deep-sea carbonates in the Red Sea. SEPM J. Sediment. Res. 39, 724–736. https://doi.org/10.1306/74d71cfd-2b21-11d7-8648000102c1865d.
Mulitza, S., Prange, M., Stuut, J.B., Zabel, M., Von Dobeneck, T., Itambi, A.C., Nizou, J., Schulz, M., Wefer, G., 2008. Sahel megadroughts triggered by glacial slowdowns of Atlantic meridional overturning. Paleoceanography 23, 1–11. https://doi.org/10.1029/2008PA001637.
Neumann, A.C., McGill, D.A., 1961. Circulation of the Red Sea in early summer. Deep Sea Res. 8, 223–235. https://doi.org/10.1016/0146-6313(61)90023-5.
Nicholson, S.E., 2018. The ITCZ and the seasonal cycle over equatorial Africa. Bull. Am. Meteorol. Soc. 99, 337–348. https://doi.org/10.1175/BAMS-D-16-0287.1.
Nicholson, S.L., Pike, A.W.G., Hosfield, R., Roberts, N., Sahy, D., Woodhead, J., Cheng, H., Edwards, R.L., Affolter, S., Leuenberger, M., Burns, S.J., Matter, A., Fleitmann, D., 2020. Pluvial periods in Southern Arabia over the last 1.1 million-years. Quat. Sci. Rev. 229. https://doi.org/10.1016/j.quascirev.2019.106112.
Palchan, D., Stein, M., Almogi-Labin, A., Erel, Y., Goldstein, S.L., 2013. Dust transport and synoptic conditions over the Sahara-Arabia deserts during the MIS6/5 and 2/1 transitions from grain-size, chemical and isotopic properties of Red Sea cores. Earth Planet Sci. Lett. 382, 125–139. https://doi.org/10.1016/j.epsl.2013.09.013.

Palchan, D., Stein, M., Goldstein, S.L., Almogi-Labin, A., Tirosh, O., Erel, Y., 2018. Synoptic conditions of fine-particle transport to the last interglacial Red Sea-Dead Sea from Nd-Sr compositions of sediment cores. Quat. Sci. Rev. 179, 123–136. https://doi.org/10.1016/j.quascirev.2017.09.004.

Palchan, D., Torfstein, A., 2019. A drop in Sahara dust fluxes records the northern limits of the African Humid Period. Nat. Commun. 10, 1–14. https://doi.org/10.1038/s41467-019-11701-z.

Parton, A., Clark-Balzan, L., Parker, A.G., Preston, G.W., Sung, W.W., Breeze, P.S., Leng, M.J., Groucutt, H.S., White, T.S., Alsharekh, A., Petraglia, M.D., 2018. Middle-late Quaternary palaeoclimate variability from lake and wetland deposits in the Nefud Desert, northern Arabia. Quat. Sci. Rev. 202, 78–97. https://doi.org/10.1016/j.quascirev.2018.10.010.

Pavlopoulos, K., Koukousioura, O., Triantaphyllou, M., Vandarakis, D., 2018. Geomorphological changes in the coastal area of Farasan Al-Kabir Island (Saudi Arabia) since mid Holocene based on a multi-proxy approach Geomorphological changes in the coastal area of Farasan Al-Kabir Island (Saudi Arabia) since mid Holocene based o. Quat. Int. 0–1. https://doi.org/10.1016/j.quaint.2018.06.004.

Petraglia, M.D., Breeze, P.S., Groucutt, H.S., 2019. Blue Arabia, green Arabia: Examining human colonisation and dispersal models. In: Rasul, N.M.A., Stewart, I.C.F. (Eds.), Geological Setting, Palaeoenvironment and Archaeology of the Red Sea, pp. 675–683. https://doi.org/10.1007/978-3-319-99408-6_30.

Pourmand, A., Marcantonio, F., Bianchi, T.S., Canuel, E.A., Waterson, E.J., 2007. A 28-ka history of sea surface tempeture, primary productivity and planktonic community variability in the western Arabian Sea. Paleoceanography 22, 1–14. https://doi.org/10.1029/2007PA001502.

Prospero, J.M., Ginoux, P., Torres, O., Nicholson, S.E., Gill, T.E., 2002. Environmental characterization of global sources of atmospheric soil dust identified with the NIMBUS 7 total ozone mapping spectrometer (TOMS) absorbing aerosol product. Rev. Geophys. 40, 1002.

R Core Team, 2022. R Core Team (2022) R: A Language and Environment for Statistical Computing. R Foundation for Statistical Computing, Vienna. https://www.R-project.org/.

Raitsos, D.E., Hoteit, I., Prihartato, P.K., Chronis, T., Triantafyllou, G., Abualnaja, Y., 2011. Abrupt warming of the Red Sea. Geophys. Res. Lett. 38. https://doi.org/10.1029/2011GL047984.

Rebolledo, L., Sepúlveda, J., Lange, C.B., Pantoja, S., Bertrand, S., Hughen, K., Figueroa, D., 2008. Late Holocene marine productivity changes in Northern Patagonia-Chile inferred from a multi-proxy analysis of Jacaf channel sediments. Estuar. Coast Shelf Sci. 80, 314–322. https://doi.org/10.1016/j.ecss.2008.08.016.

Roberts, A.P., Rohling, E.J., Grant, K.M., Larrasoaña, J.C., Liu, Q., 2011. Atmospheric dust variability from Arabia and China over the last 500,000 years. Quat. Sci. Rev. 30, 3537–3541. https://doi.org/10.1016/j.quascirev.2011.09.007.

Rohling, E.J., Fenton, M., Jorissen, F.J., Bertrand, P., Ganssen, G., Caulet, J.P., 1998. Magnitudes of sea-level lowstands of the past 500,000 years. Nature 394, 162–165. https://doi.org/10.1038/28134.

Rohling, E.J., Grant, K., Hemleben, C., Kucera, M., Roberts, A.P., Schmeltzer, I., Schulz, H., Siccha, M., Siddall, M., Trommer, G., 2008. New constraints on the timing of sea level fluctuations during early to middle marine isotope stage 3. Paleoceanography 23, 1–8. https://doi.org/10.1029/2008PA001617.

Rohling, E.J., Grant, K.M., Roberts, A.P., Larrasoaña, J.-C., Larrasoañ, J.-C., 2013. Paleoclimate variability in the mediterranean and Red Sea regions during the last 500,000 years. Curr. Anthropol. 54, S183–S201. https://doi.org/10.1086/673882.

Rojas, V.P., Meynadier, L., Colin, C., Bassinot, F., Valet, J.P., Miska, S., 2019. Multi-tracer study of continental erosion and sediment transport to the Red Sea and the Gulf of Aden during the last 20 ka. Quat. Sci. Rev. 212, 135–148. https://doi.org/10.1016/j.quascirev.2019.02.033.

Roskin, J., Tsoar, H., Porat, N., Blumberg, D.G., 2011. Palaeoclimate interpretations of Late Pleistocene vegetated linear dune mobilization episodes: evidence from the northwestern Negev dunefield, Israel. Quat. Sci. Rev. 30, 3364–3380. https://doi.org/10.1016/j.quascirev.2011.08.014.

Sakellariou, D., Rousakis, G., Panagiotopoulos, I., Morfis, I., Bailey, G., 2019. Geological structure and late quaternary geomorphological evolution of the farasan Islands continental shelf, south Red Sea, SW Saudi Arabia. In: Geological Setting, Palaeoenvironment and Archaeology of the Red Sea, pp. 629–652.

Sergiou, S., Geraga, M., Pechlivanidou, S., Gawthorpe, R.L., Ninnemann, U., Meckler, A. N., Modestou, S., Angelopoulou, D., Antoniou, D., Diz, P., McNeill, L., Shillington, D. J., Papatheodorou, G., 2024. Stratigraphic and paleoceanographic alternations within a mediterranean semi-enclosed, syn-rift basin during marine isotope stage 5: the Gulf of Corinth, Greece. Mar. Geol. 474, 107340. https://doi.org/10.1016/j.margeo.2024.107340.

Sergiou, S., Geraga, M., Rohling, E.J., Rodríguez-Sanz, L., Hadjisolomou, E., Paraschos, F., Sakellariou, D., Bailey, G., 2022a. Influences of sea level changes and the South Asian Monsoon on southern Red Sea oceanography over the last 30 ka. Quat. Res. (United States) 1–19. https://doi.org/10.1017/qua.2022.16.

Sergiou, S., Geraga, M., Rohling, E.J., Rodríguez-Sanz, L., Prandekou, A., Noti, A., Paraschos, F., Sakellariou, D., Bailey, G.N., 2022b. Marine Micropaleontology the evolution of seafloor environmental conditions in the southern Red Sea continental shelf during the last 30 ka. Mar. Micropaleontol. 177, 102181. https://doi.org/10.1016/j.marmicro.2022.102181.

Shanahan, T.M., Mckay, N.P., Hughen, K.A., Overpeck, J.T., Otto-Bliesner, B., Heil, C.W., King, J., Scholz, C.A., Peck, J., 2015. The time-transgressive termination of the African humid period. Nat. Geosci. 8, 140–144. https://doi.org/10.1038/ngeo2329.

Siani, G., Paterne, M., Arnold, M., Bard, E., Métivier, B., Tisnerat, N., Bassinot, F., 2000. Radiocarbon reservoir ages in the mediterranean Sea and black sea. Radiocarbon 42, 271–280. https://doi.org/10.1017/S0033822200059075.

Siddall, M., Rohling, E.J., Almogi-Labin, A., Hemleben, C., Meischner, D., Schmelzer, I., Smeed, D.A., 2003. Sea-level fluctuations during the last glacial cycle. Nature 423, 853–858. https://doi.org/10.1038/nature01690.

Siddall, M., Smeed, D.A., Hemleben, C., Rohling, E.J., Schmelzer, I., Peltier, W.R., 2004. Understanding the Red Sea response to sea level. Earth Planet Sci. Lett. 225, 421–434. https://doi.org/10.1016/j.epsl.2004.06.008.

Singh, A., Paul, D., Sinha, R., Thomsen, K.J., Gupta, S., 2016. Geochemistry of buried river sediments from Ghaggar Plains, NW India: multi-proxy records of variations in provenance, paleoclimate, and paleovegetation patterns in the Late Quaternary. Palaeogeogr. Palaeoclimatol. Palaeoecol. 449, 85–100. https://doi.org/10.1016/j.palaeo.2016.02.012.

Sirocko, F., Lange, H., 1991. Clay-mineral accumulation rates in the Arabian Sea during the late quaternary. Mar. Geol. 97, 105–119. https://doi.org/10.1016/0025-3227(91)90021-U.

Sirocko, F., Sarnthein, M., Erlenkeuser, H., Lange, H., Arnold, M., Duplessy, J.C., 1993. Century-scale events in monsoonal climate over the past 24,000 years. Nature 364, 322–324. https://doi.org/10.1038/364322a0.

Sirocko, F., Sirocko, F., Devey, C., Garbe-Schönberg, D., 2000. Processes controlling trace element geochemistry of Arabian Sea sediments during the last 25,000 years. Glob. Planet. Change. https://doi.org/10.1016/S0921-8181(00)00046-1.

Southon, J., Kashgarian, M., Fontugne, M., Metivier, B., Yim, Wyss W-S, 2002. Marine reservoir corrections for the Indian Ocean and southeast Asia. Radiocarbon 44, 167–180.

Stager, J.C., Ryves, D.B., Chase, B.M., Pausata, F.S.R., 2011. Catastrophic drought in the Afro-Asian monsoon region during Heinrich event 1. Science 331, 1299–1302. https://doi.org/10.1126/science.1198322.

Stein, M., Almogi-Labin, A., Goldstein, S.L., Hemleben, C., Starinsky, A., 2007. Late Quaternary changes in desert dust inputs to the Red Sea and Gulf of Aden from 87Sr/86Sr ratios in deep-sea cores. Earth Planet Sci. Lett. 261, 104–119. https://doi.org/10.1016/j.epsl.2007.06.008.

Stein, M., Hofmann, A.W., 1992. Fossil plume head beneath the Arabian lithosphere? Earth Planet Sci. Lett. 114, 193–209. https://doi.org/10.1016/0012-821X(92)90161-N.

Sun, D., Bloemendal, J., Rea, D.K., Vandenberghe, J., Jiang, F., An, Z., Su, R., 2002. Grain-size distribution function of polymodal sediments in hydraulic and aeolian environments, and numerical partitioning of the sedimentary components. Sediment. Geol. 152, 263–277. https://doi.org/10.1016/S0037-0738(02)00082-9.

Sunagawa, I., Takahashi, Y., Imai, H., 2007. Strontium and aragonite-calcite precipitation. J. Mineral. Petrol. Sci. 102, 174–181. https://doi.org/10.2465/jmps.060327a.

Thunell, R.C., Locke, S., Williams, D.F., 1988. Glacio-eustatic Sea-Level Control on Red Sea Salinity.

Tierney, J.E., DeMenocal, P.B., 2013. Abrupt shifts in Horn of Africa hydroclimate since the last glacial maximum. Science 342, 843–846. https://doi.org/10.1126/science.1240411.

Tierney, J.E., deMenocal, P.B., Zander, P.D., 2017. A climatic context for the out-of-Africa migration. Geology 45 (1), 1023–1026. https://doi.org/10.1130/G39457.

Trommer, G., Siccha, M., Rohling, E.J., Grant, K., Meer, M.T.J. Van Der, Schouten, S., Hemleben, C., Kucera, M., Schouten, S., van der Meer, M.T.J., Hemleben, C., Grant, K., Rohling, E.J., Siccha, M., Trommer, G., 2010. Millennial - scale variability in Red Sea circulation in response to Holocene insolation forcing. Paleoceanography 25, 1–17. https://doi.org/10.1029/2009PA001826.

Trommer, G., Siccha, M., Rohling, E.J., Grant, K., Van Der Meer, M.T.J., Schouten, S., Baranowski, U., Kucera, M., 2011. Sensitivity of Red Sea circulation to sea level and insolation forcing during the last interglacial. Clim. Past 7, 941–955. https://doi.org/10.5194/cp-7-941-2011.

Van Rampelbergh, M., Fleitmann, D., Verheyden, S., Cheng, H., Edwards, L., De Geest, P., De Vleeschouwer, D., Burns, S.J., Matter, A., Claeys, P., Keppens, E., 2013. Mid- to late Holocene Indian ocean monsoon variability recorded in four speleothems from socotra Island, Yemen. Quat. Sci. Rev. 65, 129–142. https://doi.org/10.1016/j.quascirev.2013.01.016.

Weikert, H., 1982. The vertical distribution of zooplankton in relation to habitat zones in the area of the atlantis II deep, central Red Sea. Mar. Ecol. Prog. Ser. 8, 129–143. https://doi.org/10.3354/meps008129.

Weltje, G.J., 1997. End-member modeling of compositional data: numerical-statistical algorithms for solving the explicit mixing problem. Math. Geol. 29, 503–549. https://doi.org/10.1007/bf02775085.

Weltje, G.J., Bloemsma, M.R., Tjallingii, R., Heslop, D., Croudace, I.W., Tjallingii, R., Röhl, U., Heslop, D., Weltje, G.J., 2015. Prediction of geochemical composition from XRF core scanner data : a new multivariate approach including automatic selection of calibration samples and quantification of uncertainties 507–534. https://doi.org/10.1007/978-94-017-9849-5.

Weltje, G.J., Tjallingii, R., 2008. Calibration of XRF core scanners for quantitative geochemical logging of sediment cores: theory and application. Earth Planet Sci. Lett. 274, 423–438. https://doi.org/10.1016/j.epsl.2008.07.054.

Werner, F., Lange, K., 1975. A bathymetry survey of the sill area between the Red Sea and Gulf of Aden. Geol. Jahrb. D, 25–30.

Williams, S.J., 2013. Sea-level rise implications for coastal regions. J. Coast Res. 63 (1), 184–196. https://doi.org/10.2112/SI63-015.

Ziegler, M., Jilbert, T., De Lange, G.J., Lourens, L.J., Reichart, G.J., 2008. Bromine counts from XRF scanning as an estimate of the marine organic carbon content of sediment cores. Geochemistry, Geophys. Geosystems 9, 1–6. https://doi.org/10.1029/2007GC001932.